Measurement of particle accelerations in fully developed turbulence

By GREG A. VOTH, A. LA PORTA,
ALICE M. CRAWFORD, JIM ALEXANDER
AND EBERHARD BODENSCHATZ

Laboratory of Atomic and Solid State Physics, Laboratory of Nuclear Studies, Cornell University,
Ithaca, NY 14853, USA

We use silicon strip detectors (originally developed for the CLEO III high-energy particle physics experiment) to measure fluid particle trajectories in turbulence with temporal resolution of up to 70 000 frames per second. This high frame rate allows the Kolmogorov time scale of a turbulent water flow to be fully resolved for $140 \geqslant R_\lambda \geqslant 970$. Particle trajectories exhibiting accelerations up to $16\,000\,\mathrm{m\,s^{-2}}$ (40 times the r.m.s. value) are routinely observed. The probability density function of the acceleration is found to have Reynolds-number-dependent stretched exponential tails. The moments of the acceleration distribution are calculated. The scaling of the acceleration component variance with the energy dissipation is found to be consistent with the results for low-Reynolds-number direct numerical simulations, and with the K41-based Heisenberg–Yaglom prediction for $R_\lambda \geqslant 500$. The acceleration flatness is found to increase with Reynolds number, and to exceed 60 at $R_\lambda = 970$. The coupling of the acceleration to the large-scale anisotropy is found to be large at low Reynolds number and to decrease as the Reynolds number increases, but to persist at all Reynolds numbers measured. The dependence of the acceleration variance on the size and density of the tracer particles is measured. The autocorrelation function of an acceleration component is measured, and is found to scale with the Kolmogorov time τ_η.

1. Introduction

Fluid turbulence may be characterized in terms of variables defined at points fixed in space (the Eulerian reference frame), or in terms of the trajectories of fluid particles (the Lagrangian reference frame). This distinction applies both to theoretical formulations of turbulence and to experimental techniques for characterizing turbulent flows. Although the formulation of fluid dynamics is generally considered to be more tractable in terms of Eulerian variables, the critical issues of transport and mixing in turbulence are more directly related to the properties of fluid trajectories (Shraiman & Siggia 2000; Yeung 2001*b*; Sawford 2001), and are often addressed using Lagrangian techniques (Pope 1994). There are also many applications in which the transport or aggregation of particulate matter in turbulence is important in its own right, such as water droplet aggregation in clouds (Vaillancourt & Yau 2000) or the industrial production of nanoparticles (Pratsinis & Srinivas 1996).

In a basic sense, data obtained from Lagrangian and Eulerian measurements are complementary. In the Eulerian frame, one is typically concerned with differences

between quantities (velocity component, scalar concentration, etc.) measured at several points separated by a fixed distance in space. It would be equally interesting to study time differences; however making such measurements within the Eulerian framework is difficult (Kit, Tsinober & Dracos 1993). The true temporal structure of turbulence is revealed when fluctuations are measured along a particle trajectory, in the Lagrangian frame.

Turbulence has traditionally been studied in the Eulerian frame rather than the Lagrangian frame for technical reasons. The hot-wire anemometer used in conjunction with the Taylor frozen flow hypothesis provides extremely accurate Eulerian data in turbulent gas flows over a broad range of Reynolds number, but no comparably effective technique has been available for Lagrangian measurements. However, as the range of Reynolds number accessible to direct numerical simulations (DNS) of turbulence has expanded, numerical studies of particle trajectories in isotropic turbulence have yielded important insights (Yeung & Pope 1989; Vedula & Yeung 1999; Yeung 2001a; Gotoh & Rogallo 1999; Gotoh & Fukayama 2001). Although very little experimental data for Lagrangian properties in fully developed turbulence has been available, this is beginning to change. Basic issues, such as the Richardson law for particle dispersion (Monin & Yaglom 1975), the Heisenberg–Yaglom prediction of fluid particle accelerations (Heisenberg 1948; Yaglom 1949), and Kolmogorov scaling of temporal velocity differences have remained untested for many decades. Recent experiments by Voth, Satyanarayan & Bodenschatz (1998), Ott & Mann (2000), La Porta *et al.* (2001), and Mordant *et al.* (2001) have made significant progress in addressing each of these but there are still major limitations. In particular, limitations in spatial and temporal measurement resolution have obscured the small scales at large Reynolds number. More complete information about particle trajectories in real (non-idealized) turbulent flows is needed to guide the development of models of transport in applications (Pope 1994).

In principle, fluid particle trajectories are easily measured by seeding a turbulent flow with minute tracer particles and following their three-dimensional motions with an imaging system. In practice, this is a very challenging task because changes in particle velocity or acceleration can take place on time scales of order of the Kolmogorov time, $\tau_\eta = (v/\epsilon)^{1/2}$ where v is the kinematic viscosity and ϵ is the energy dissipation per unit mass. In order to observe universal scaling behaviour we require that the Reynolds number, defined by $Re = uL/v$, where u is the r.m.s. velocity and L is the energy injection scale, approach 10^5. (This is equivalent to requiring that the Taylor microscale Reynolds number $R_\lambda = (15Re)^{1/2}$ approach 1000.) In a laboratory water flow ($v \approx 10^{-6}\,\mathrm{m^2\,s}$) with a convenient energy injection scale ($L \approx 0.1\,\mathrm{m}$) and assuming $\epsilon = u^3/L$ we must have $\epsilon \approx 10\,\mathrm{m^2\,s^{-3}}$, which implies $\tau_\eta \approx 0.3\,\mathrm{ms}$. In order to measure particle accelerations, motions which take place over this time scale must be fully resolved.

Although conventional imaging systems based on charge coupled devices (CCD) have been used for three-dimensional tracking of particles in low-Reynolds-number flows (Snyder & Lumley 1971; Sato & Yamamoto 1987; Virant & Dracos 1997; Ott & Mann 2000) they do not provide adequate temporal resolution for use in fully developed turbulence, as specified above. However, these requirements may be met by the use of silicon strip detectors as optical imaging elements in a particle tracking system. The strip detectors used in our experiment were developed to measure sub-atomic particle tracks in the vertex detector of the CLEO III experiment operating at the Cornell Electron-Positron Collider (Skubic *et al.* 1998). When applied to particle tracking in turbulence each detector measures a one-dimensional projection of the

image of the tracer particles. Using a data acquisition system designed specifically for the turbulence experiment several detectors may be simultaneously read out at 70 000 frames per second, making it possible to measure two-dimensional or three-dimensional particle trajectories with very high spatial and time resolution (Voth *et al.* 2001; La Porta *et al.* 2001).

The technical demands of particle tracking in turbulence and the scope of phenomena which become accessible when these demands are met can best be appreciated by examining one of the more dramatic particle trajectories recorded with the strip detector particle tracking system. The three-dimensional trajectory shown in figure 1 was recorded in a flow between counter-rotating disks at $R_\lambda = 970$ (described below in §3) having an r.m.s. velocity of approximately $1 \, \mathrm{m \, s^{-1}}$, a Kolmogorov time τ_η of approximately $0.3 \, \mathrm{ms}$, and a Kolmogorov distance scale η of $20 \, \mu\mathrm{m}$.

The trajectory was recorded at 70 000 frames per second using a pair of strip detectors collecting primary and conjugate charge, as will be described in §2 below. The particle enters the measurement volume near the top right of figure 1 and appears to be trapped in a vortical structure. In the third, tightest turn of the helical motion the acceleration of the particle rises to $16\,000 \, \mathrm{m \, s^{-2}}$ within a time interval of $0.5 \, \mathrm{ms}$ ($\approx 1.5\tau_\eta$). During this trajectory the velocity components of the particle, shown in figure 2, oscillate wildly, spanning a range considerably larger than the r.m.s. velocity within a Kolmogorov time. The extreme fluctuations in velocity and acceleration, which occur on time scales of order of the Kolmogorov time, make great demands on the particle tracking system.

The trajectory in figures 1 and 2 is also noteworthy in that it seems to lie outside the characteristic range of the energy cascade. For the first part of the trajectory the particle appears to be caught in a very intense vortical structure. The tightest loop in the helical trajectory of the particle is about $300 \, \mu\mathrm{m}$ in diameter, or about 15η, which is in the inertial subrange quite close to the dissipative scale of the turbulence. The period of the motion appears to be less than $1 \, \mathrm{ms}$, of the order of the Kolmogorov time τ_η. Yet the velocity fluctuations observed in this trajectory exceed the r.m.s. velocity, which would normally be associated with the largest scales of the turbulence (the so called energy-containing range). Events of this nature, which up until now were experimentally inaccessible, may be interpreted as a manifestation of turbulent intermittency.

The remainder of the paper is organized as follows. In §2 the operating principles and capabilities of the particle tracking system based on a silicon strip detector are discussed. This includes discussion of the optical system used to image the tracer particles on the strip detector (§2.2). In §3 the turbulent water flow between counter-rotating disks is described, and characterized using the silicon strip detector. This entails measurement of the velocity statistics and an estimate of the energy dissipation from the transverse-velocity structure function.

The main results are the investigation of the statistics of particle accelerations in turbulence for $140 \leqslant R_\lambda \leqslant 970$, given in §4. (A brief account of part of this research has previously been published in La Porta *et al.* 2001.) In §4.1 the probability density function (PDF) of the acceleration component is measured as a function of Reynolds number and component direction. In §4.2 the scaling of the acceleration component variance is compared with the Heisenberg–Yaglom prediction. It is found that the data are consistent with DNS results at low Reynolds number, and with the Heisenberg–Yaglom predicted scaling for $R_\lambda \geqslant 500$. The flatness of the acceleration component is found to be quite large and to increase with Reynolds number, exceeding 60 at $R_\lambda = 970$. The acceleration component autocorrelation function is shown in §4.4.
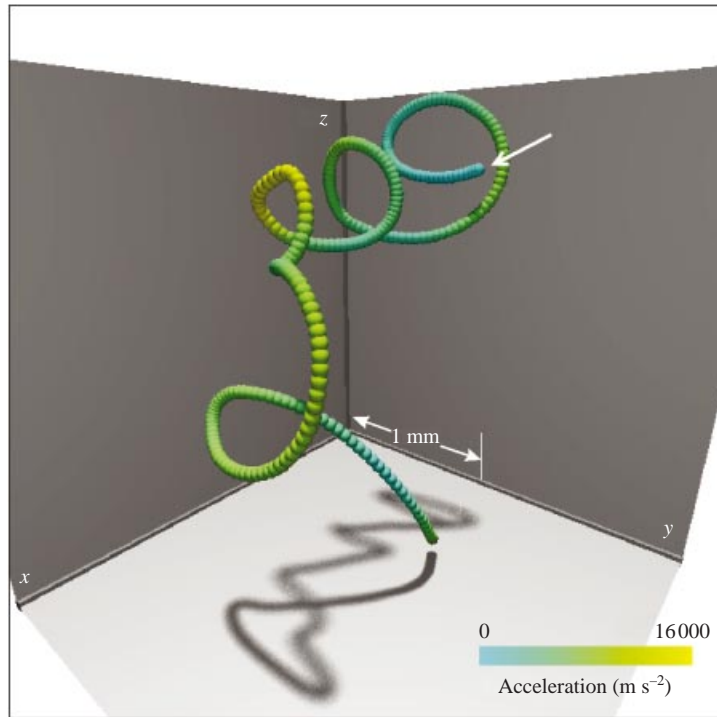
FIGURE 1. Trajectory of a 46 μm diameter tracer particle in turbulence at $R_\lambda = 970$ recorded at frame rate 70 000 f.p.s. The position of the particle at each of 278 frames is represented as a sphere. The acceleration magnitude is represented by the colour of the trajectory, as indicated by the scale. The maximum acceleration shown corresponds to about 30 standard deviations from the mean.
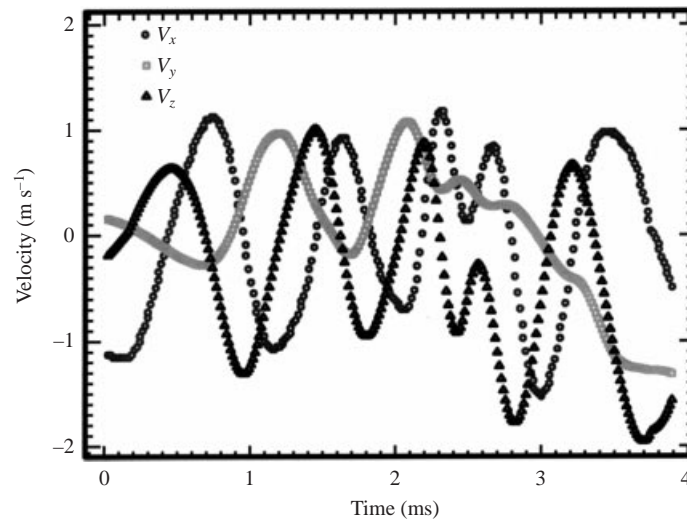

FIGURE 2. Three components of the velocity of the particle shown in figure 1.

The autocorrelation function is shown to scale with the Kolmogorov time. Finally, the influence of particle size and density are studied in §5. It is found that the acceleration of relatively large particles (diameter $\geqslant 5\eta$) can be significantly smaller than that of infinitesimal fluid particles, and that, in this experiment, particle size and
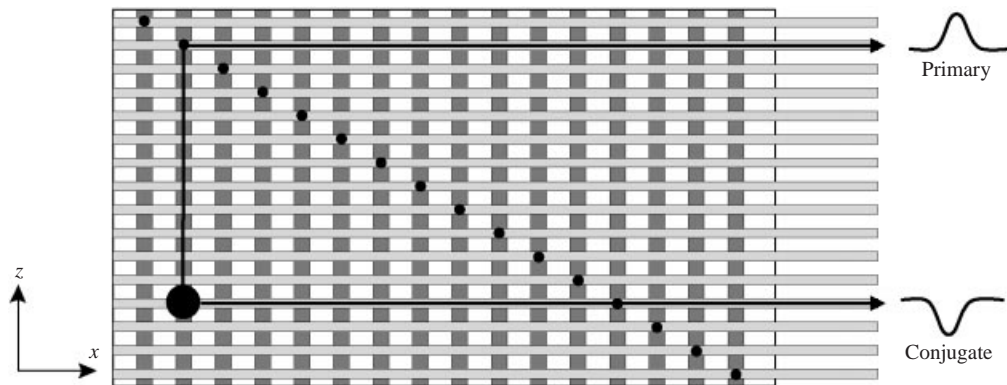
FIGURE 3. Simplified schematic of the strip detector. Dark grey bars represent p-type sense strips. Light grey bars superimposed on the dark bars represent metal leads evaporated on to the surface of the detector. The small circles along the diagonal represent paths that connect sense strips to the leads. Under normal circumstances, only 'primary' charge is collected indicating the x-coordinate of light spots incident on the detector. However, the detector bias may be adjusted so that 'conjugate' charge is also detected by the metal leads indicating the z-coordinate, as described in the text.

not density is primarily responsible for this. However, the acceleration variance of the 46 μm particles used for the acceleration measurements differs from that of ideal fluid particles by only a few percent. Two appendices are also included. The first details the algorithms used for extracting particle tracks from the strip detector output, and the second compares the results published here with previous measurements, which were made with a conventional detection system which had much lower resolution.

2. Particle tracking system

2.1. *Strip detector*

A brief description of the the strip detector tracking system is provided below. It is described in detail in Voth *et al.* (2001).

The silicon strip detector is essentially a large planar photodiode (sensitive area 51 mm × 25.6 mm) which is segmented into 512 sense strips, as shown in figure 3. Optical radiation incident on the detector creates electron–hole pairs, and the holes are collected by p-type strips patterned on the front surface of the n-type detector. Charge is conducted off the detector chip through metallic leads evaporated onto the surface of the detector which are oriented perpendicular to the sense strips. The positive charge collected by the array of strips gives a one-dimensional projection of the light intensity incident on the detector, allowing the x-coordinate of a particle that is imaged onto the detector to be measured. However, for certain settings of the detector bias, electrons appear to become trapped in meta-stable surface states and couple capacitively to the metallic leads. Under these circumstances, negative 'conjugate' charge indicates the projection of the intensity on the axis defined by the leads (which is perpendicular to the axis defined by the sense strips). By distinguishing the primary (positive) and conjugate (negative) peaks the two-dimensional projection of a particle trajectory may be measured using a single detector. Positions measured from conjugate charge have greater uncertainty, so for most of the data presented below, and in particular for the acceleration measurements, primary charge was used for position measurement.
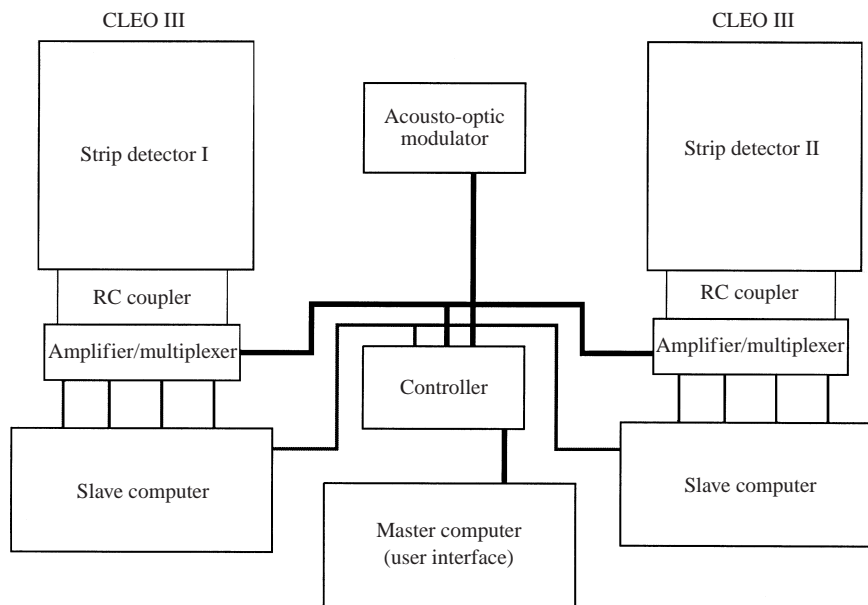
FIGURE 4. The readout cluster. Each strip detector is read out using an individual slave computer. A field programmable gate array (FPGA) detector controller generates timing signals for the strip detector data acquisition hardware, and acousto-optic modulator. A master computer controls the slave computers via Ethernet messaging and provides the user interface for the system.

As shown in figure 4, the 512 strips of each strip detector are connected to an array of four resistor–capacitor (RC) chips which provide an individual bias resistor and coupling capacitor for each channel. The output capacitors are connected to an array of four integrated amplifier/multiplexer chips, which provide a shaper amplifier and sample-and-hold amplifier for each strip. After a frame of data is latched on the array of sample and hold amplifiers, analog multiplexers integrated into the amplifier chips output the strip intensities as four 10 M sample/s waveforms. A detector controller generates frame-readout triggers for the strip detectors, readout electronics and an acousto-optic modulator, and may be configured for readout rates in the range 5 kHz– 70 kHz. The acousto-optic modulator is used to strobe the illumination before the readout of each frame, which is necessary to optimally drive the shaper amplifiers. The output waveforms are captured using a pair of dual-channel digital oscilloscope boards mounted in a PCI bus slave computer. The oscilloscope boards can store 4000 frames of data in internal memory, which is subsequently downloaded into the computer's main memory. The slave computer performs pedestal subtraction, thresholding, and stores compressed data on a local hard disk concurrently with the acquisition of the next frame of data. The maximum duration of continuous acquisition ranges from 800 ms at 5 kHz to 58 ms at 70 kHz. The time required to process and store one 4000 frame sequence is approximately 1 s, and this limits the duty cycle of the acquisition system at high frame rates.

2.2. *Optical imaging system*

The optical configuration used to image particles is shown in figure 5. The illumination beam, generated by a 6 W continuous wave argon-ion laser and gated by the acousto-optic modulator, is directed through a glass window and passes through the centre of the flow chamber. The beam is a TM_{00} Gaussian mode and a beam expander
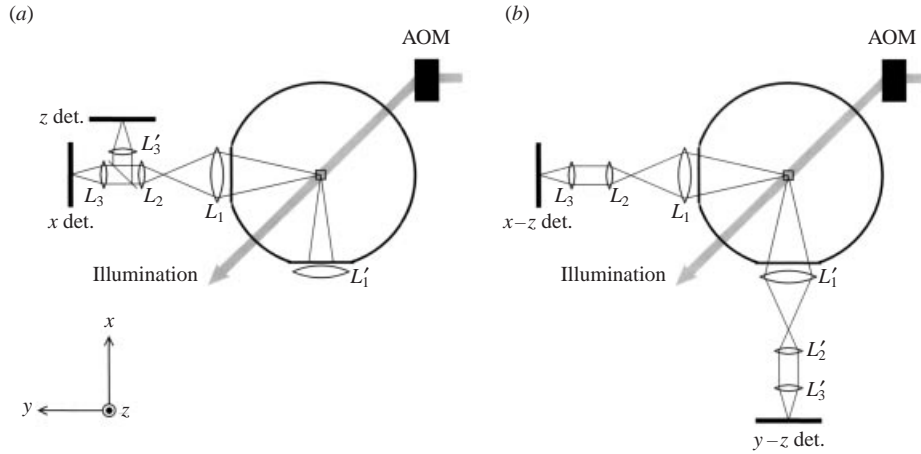
FIGURE 5. (*a*) Optical layout for acceleration measurements, viewed along the axis of the cylindrical turbulence chamber ($\hat{z}$). The illumination beam is gated by an acousto-optic modulation (AOM) before being passed through the centre of the turbulence chamber. Optics are used to image the central volume through a view-port at 45° with respect to the illumination. A beam-splitter allows the image to be projected on two strip detectors which are oriented to measure two orthogonal coordinates. An additional view-port may also be used to measure the third coordinate. (*b*) Optical layout for three-dimensional particle measurement. The apparatus is the same except that imaging optics are present on both ports. In this case strip detectors are operated with conjugate peaks enabled (see text) so each port has a detector which measures two position coordinates.

is used to obtain a spot radius $\omega \approx 1.0$ mm with negligible divergence. This beam radius is chosen so that the beam fills the field of view of the detector, in this case approximately 2 mm. Acceleration measurements were taken in the configuration shown in figure 5(*a*), in which two strip detectors view a common image and measure two-dimensional coordinates. Some three-dimensional tracks were recorded in the configuration shown in figure 5(*b*), in which two detectors view the volume from different view-ports so that their detection volumes overlap.

The design of the imaging system sketched in figure 5 is determined by the requirement that a small measurement volume be imaged at high magnification by optics which are placed outside the turbulence chamber. These design requirements were met by the two stage imaging system shown in figure 6(*a*). In order to maintain acceptable depth of field, the aperture shown after the first imaging lens (L1 in figure 6) is used to restrict the numerical aperture of the imaging system to a value of 0.03, giving a spot size $\approx 300\,\mu$m for images of particles throughout the measurement volume. As a result, at least three strips were illuminated by each particle image, making it possible to locate the particle with sub-strip resolution by fitting each peak to a Gaussian function.

Although the magnification of the optical system defined in figure 6 is nominally f_3/f_2, it is useful to vary the configuration of the system in order to adjust the magnification and position of the focal plane. In particular, L_1 may be repositioned to change the magnification of the first stage of the system, and L_3 is replaced by a pair of lenses whose separation-dependent effective focal length replaces f_3. For the acceleration data presented below, L_1 is a compensated doublet with focal length 15 cm, L_2 is a doublet of focal length 3.8 cm and L_3 is replaced by a pair of lenses consisting of a 30 cm focal length plano-convex lens and a -50 cm plano-concave lens separated by approximately 10 cm. The detector is placed approximately 25 cm
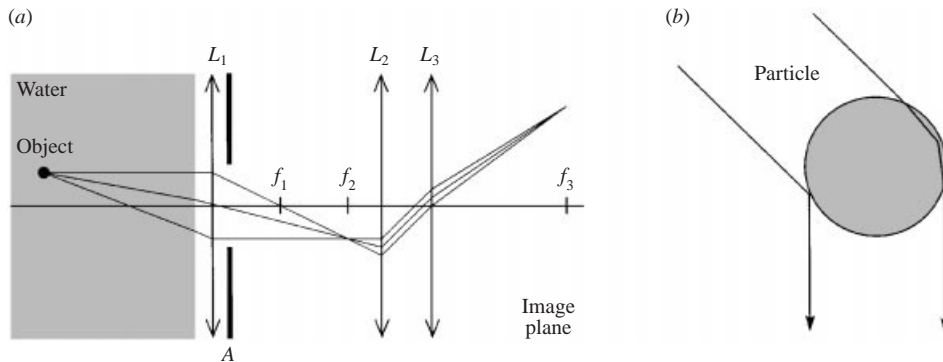
(*a*)

(*b*)

FIGURE 6. A simplified schematic of the optical system is shown. (*a*) Plano-convex lens L_1 is place just outside the fluid chamber and is used to image the active volume with 1 : 1 magnification. A short-focal-length lens L_2 is positioned so that its front focal plane (f_2) lies at the centre of the image formed by L_1. As a result, point sources in the image are transformed into parallel ray bundles by L_2. The bundles are focused by L_3 at its rear focal plane (f_3). A beam splitter may be inserted between L_2 and L_3 to allow the image to be projected on a second detector, as shown in figure 5. The magnification of the system is given by the ratio of the focal lengths f_3/f_2. The light collection of the imaging system is controlled by an aperture placed behind lens L_1. (*b*) The tracer particles are transparent polystyrene spheres with density $1.06 \, \mathrm{g\,cm^{-3}}$ and diameter $46 \, \mu\mathrm{m}$ and are detected via specular reflection from the internal and external surfaces. With illumination at $45°$ and polarization perpendicular to the plane of incidence, the internal reflection is much stronger than the external reflection so that the particle appears as a single point-like source of light.

behind the plano-concave lens. The magnification of the system is approximately 12.8, so that the $100 \, \mu\mathrm{m}$ pitch of the strip detector corresponds to approximately $7.8 \, \mu\mathrm{m}$ in the fluid volume, giving a field of view of $2.00 \, \mathrm{mm} \times 4.00 \, \mathrm{mm}$. The effective magnification of the system is measured to within 2% using a calibration target that is positioned in the active region at the centre of the flow chamber. (The variation of the magnification is less than 1% over the illuminated volume, so it was not necessary to express the magnification as a function of depth.)

For acceleration data, the strip detectors have the reverse voltage bias set such that conjugate charge is suppressed, allowing them to measure a single coordinate using the primary charge signal. In order to measure two-dimensional trajectories, a beam-splitter is used to project the same image onto two detectors (see figure 5*a*), which are oriented to measure orthogonal coordinates. Because of the 2 : 1 aspect ratio of the detector, the fields of view of the two detectors do not coincide, as shown in figure 7. In this case, the full area of each detector can be used to measure one-dimensional trajectories, but two-dimensional trajectories can only be measured in the region where the two fields overlap. As a result, only half of the 512 strips are available when analysing two-dimensional trajectories.

2.3. *Determination and characterization of tracks*

Data files stored by the experiment consist of thresholded intensity data simultaneously acquired by the two strip detectors. These data files are passed through several stages of analysis. This task is similar in principle to that employed in standard particle tracking studies using CCD cameras, but the algorithms employed must be tailored to the peculiar characteristics of one-dimensional projection images. Figure 8 shows a two-dimensional particle track which has been constructed from raw data. A description of the algorithm used for track extraction is given in Appendix A.
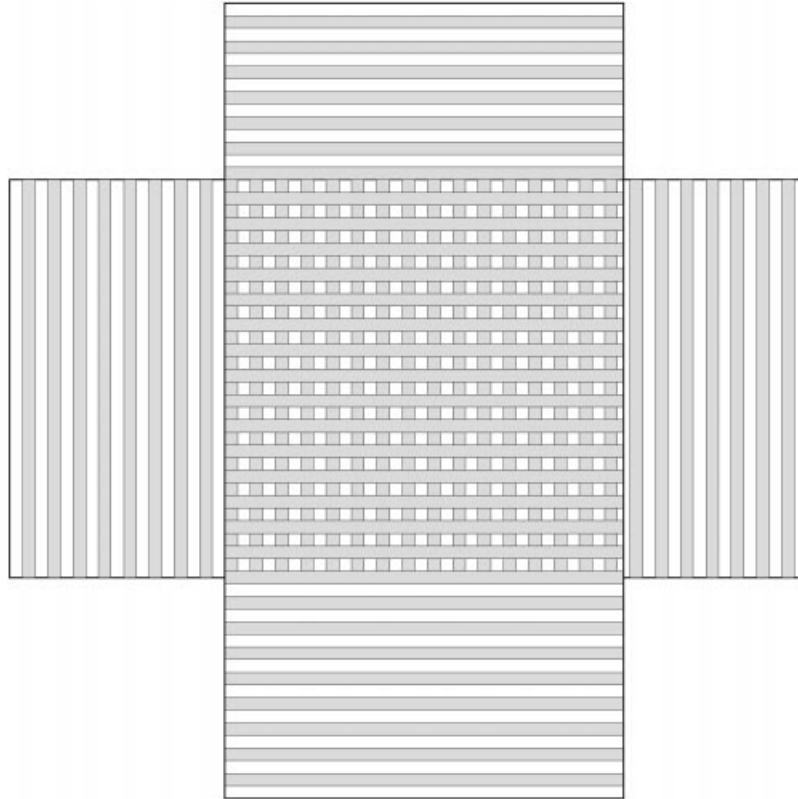
FIGURE 7. The relative fields of view of two strip detectors oriented as in figure 5(*a*) to measure perpendicular coordinates, where the grey stripes represent the orientation of the charge-collecting sense strips. Because of the 2 : 1 aspect ratio of the detector, only half of the field of each detector overlaps with the field of the other, so that only 256 strips can be used for coincident measurements.

Secondary data files, consisting of lists of tracks measured for each data sequence are stored for subsequent analysis.

The accuracy of the particle positions is estimated by fitting a straight line to very short track segments (shorter than τ_η) and measuring the mean deviation between the data points and the fit. The deviation is found to depend most significantly on the peak height. Figure 9 shows the error as a function of peak height for a typical run. For extremely weak peaks (maximum intensity < 0.02 V) the error can be of order 1/2 a strip, but the the analysis routines are configured to limit the data to larger intensity, so that the mean error is $\leqslant 0.1$ strips. The error for individual trajectories can vary depending on focus and aperture, but always remains below 0.2 strips.

The frame period, $\Delta\tau$, and the number of measurements per Kolmogorov time $\tau_\eta/\Delta t$, are tabulated for each *Re* in table 2 (§4.2). Δt is chosen for most *Re* so that on average the particles travel approximately 6 μm or 0.7 strips between frames. The very highest and lowest *Re* are limited by the maximum and minimum allowable frame rates and so have an average travel between frames of 12 μm or 1.5 strips and 4 μm or 0.5 strips respectively.

One can also consider the mean deviation of the peak from the linear fit as a function of the position (in strips) modulo 1, shown in figure 10. The dependence of the mean deviation on the position indicates a nonlinearity in the interpolation of the
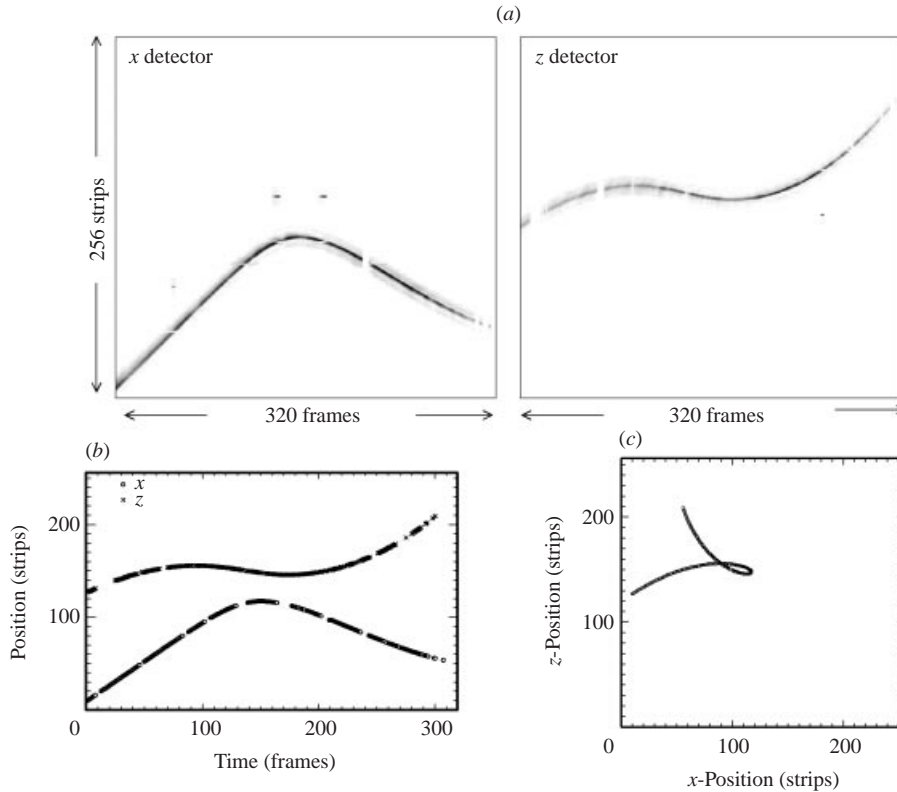
FIGURE 8. (*a*) Raw data from the two strip detectors. Only the 256 overlapping strip segments are shown. (*b*) Positions vs. time measured from the raw data, where gaps are due to the presence of inoperative strips. (*c*) Reconstruction of the two-dimensional track from the position data in (*b*), where gaps have been bridged by linear interpolation.

peak centres which is smaller than, but of the same order as, the random uncertainty. This nonlinearity is compensated for by subtraction of the mean deviation from the peak positions before processing of the trajectories.

The kinematic properties of the tracks are measured by polynomial fits (parabolic for acceleration, linear for velocity) to the position vs. time data. The fits are made using the standard least-squares algorithm, with the relative weight of each data point proportional to the inverse square of the estimated error (as a function of peak intensity, figure 9). The length of track over which the fit is performed is a complex issue, which is discussed in detail below.

One of the greatest challenges in the measurement of accurate statistics of Lagrangian variables is the control of sample biases. From a physical standpoint, one must take care that the tracer particles uniformly sample the fluid volume and follow the flow field. This requires that the particles be sufficiently small and that the density match between the particle and the fluid be sufficiently close. This issue is addressed in §5, below. It is also necessary to ensure that the measurement and analysis procedures do not introduce biases in the measurements of the particle trajectories. For instance, if one were to make one measurement for each particle that enters the measurement volume, a distorted velocity distribution would be obtained, since the rate at which particles enter the measurement volume is itself proportional to the velocity of the particle (Buchave, George & Lumley 1979; Voth *et al.* 1998).
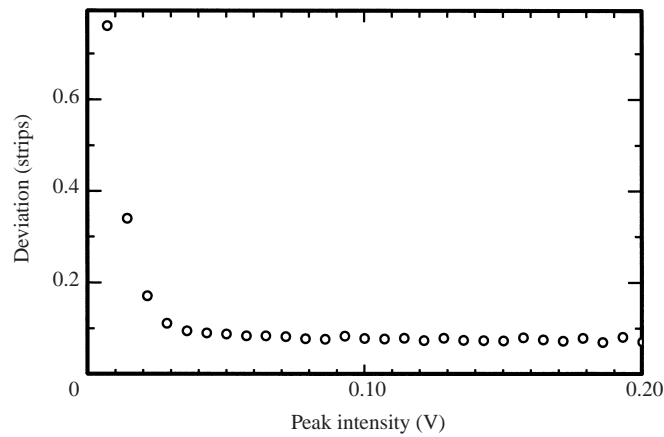
FIGURE 9. Estimate of particle position error. The graph shows the r.m.s. deviation of the peak centre from a linear fit to a short segment of track.
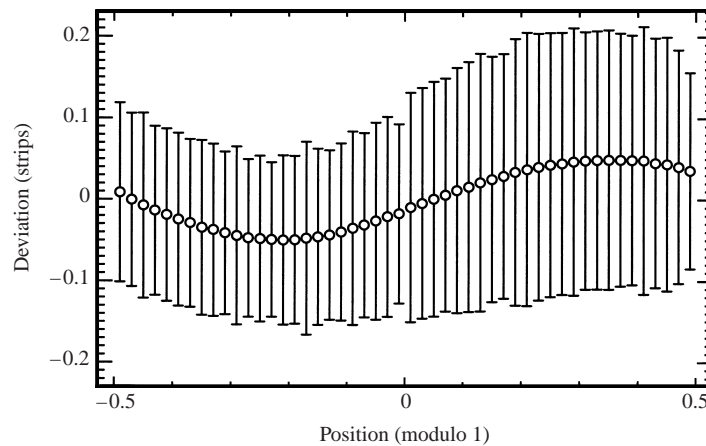

FIGURE 10. Deviation of particle position from fit as a function of position modulo 1. The circle indicates the mean and the error bars indicate the standard deviation of the deviation of the peaks from the fit.

However, the time that a particle will remain in the measurement volume is inversely proportional to the velocity, and these two factors cancel. Ideally, one would achieve uniform sampling within the measurement volume by continuously measuring the kinematic properties of the track from the time that a particle enters the volume to the time that it exits. In practice this is impossible to achieve because the acceleration and velocity are measured by fitting to a polynomial function, and so the variables cannot be measured until the particle has been in the measurement volume for a finite time. Another difficulty is that measurement is not possible when particles cross paths or traverse inoperative pixels. The strategy employed is to measure the variables as many times as possible along the trajectory, and make the total statistical weight of these measurements proportional to the total length of the track. This seems to give the best approximation of uniform sampling of the measurement volume.
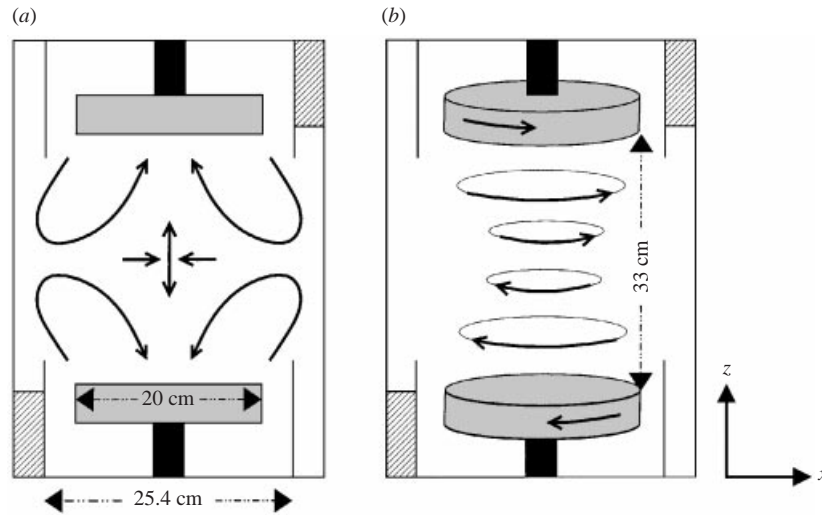
FIGURE 11. Schematic representation of the flow between counter-rotating disks decomposed into (*a*) the pumping (poloidal) mode and (*b*) the shearing (toroidal) mode.

3. Characterization of the flow

The goal of this study is to explore universal characteristics of turbulent flows. However, our flow deviates significantly from the ideal of homogeneity and isotropy. The apparatus used to generate the turbulent water flow is described in §3.1. We have used the strip-detector particle tracking system to characterize the flow in terms of standard Eulerian quantities. This includes measurement of the scaling of the r.m.s. velocity components with propeller speed (§3.2), an estimate of the rate of energy dissipation in terms of the velocity structure functions (§3.3), and measurement of the anisotropy of the mean velocity field at the centre of the flow (§3.4).

3.1. *Turbulence generator*

The turbulence is generated in a flow of water between counter-rotating disks in a cylindrical container (Voth *et al.* 1998; La Porta *et al.* 2000), as represented schematically in figure 11 and shown in figure 12. This type of flow has been widely used since Douady, Couder & Brachet (1991) made measurements in a similar apparatus (Fauve, Laroche & Castaing 1993; Maurer, Tabeling & Zocchi 1994; Cadot, Douady & Couder 1995; Belin *et al.* 1996; Aumaitre, Fauve & Pinton 2000; Mordant *et al.* 2001). The container, mounted vertically, is 48.3 cm in diameter and 60.5 cm long with eight planar windows mounted flush with the surface of the cylinder at equal angles along the mid-line of the chamber. All physical quantities are defined with reference to a Cartesian coordinate system in which the z-axis corresponds to the axis of symmetry of the cylinder and the x- and y-axes correspond to the optical axes of the two imaging systems represented in figure 5(*b*). By symmetry the two transverse coordinates (x and y) are equivalent, and distinct from the axial coordinate (z). The disk-shaped propellers are open-ended cylinders 20 cm in diameter and 4.3 cm deep with twelve internally mounted radial vanes. The propellers are spaced 33 cm apart and are each driven by 0.9 kW computer controlled dc motors that are coupled to the propellers with variable speed reducers. A cylindrical tube of diameter 25.4 cm surrounds each propeller and extends 5 cm beyond it. Stationary radial vanes between this tube and the container wall have been installed to inhibit large-scale rotation of

Figure 12. Apparatus, consisting of turbulence chamber with counter-rotating disks (foreground), illumination beam entering from foreground and two detectors (background).

the flow. For the studies described below, the propeller rotation rate is varied from 0.15 Hz to 7.0 Hz. The lower limit is set by the motors and speed reducers and the higher limit is set by the temporal resolution of the detector. (The detectors are not able to adequately resolve the Kolmogorov time at the maximum propeller speed of 9 Hz.)

The averaged flow produced by the propellers can be interpreted as a superposition of two basic components, a pumping (poloidal) mode and a shearing (toroidal) mode. Centrifugal pumping by the propellers produces the flow represented schematically in figure 11(a). The resulting mean strain field at the centre of the chamber (represented by the arrows in figure 11a) tends to enhance the axial component of the vorticity. In addition, fluid near the top and bottom of the cylinder tends to rotate collectively with the counter-rotating propellers, creating a shear layer around the edge of the flow midway between the propellers, as represented in figure 11(b). Particle accelerations are measured in a $8\,\text{mm}^3$ volume at the centre of the flow chamber. Quantitative measures of the flow, described in detail below, are derived from measurements in this volume, and additional measurements in a larger $15\,\text{mm} \times 30\,\text{mm}$ volume. More details regarding this flow are given in Voth *et al.* (1988) and La Porta *et al.* (2000). (See also Appendix B.)

3.2. *Measurement of the velocity fluctuations*

Velocity statistics may be obtained from analysis of matched trajectories obtained with the apparatus in its standard configuration, shown in figure 5(a). As mentioned above, in order to obtain a correct estimate of the r.m.s. velocity, it is necessary to take care to sample trajectories uniformly by ensuring they are continuously sampled
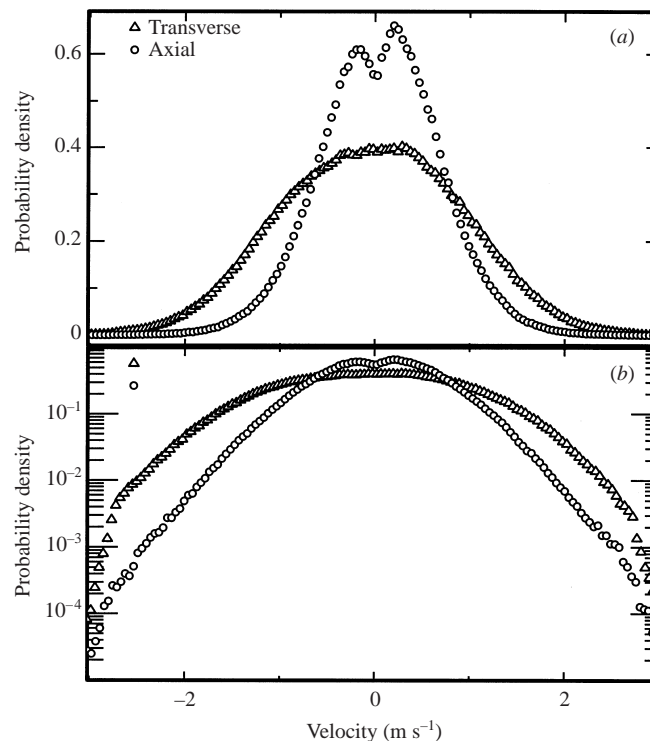
FIGURE 13. (*a*) The PDF for the velocity. (*b*) Same data as (*a*) plotted on a semi-log scale.

as long as they remain in the measurement volume. The PDF of the velocity is shown for linear and log scales in figure 13. It is evident that the standard deviation of the transverse component exceeds that of the axial component by about 50%. The distributions for both components are approximately Gaussian; the flatness is 2.8 for the axial and 3.2 for the longitudinal component. These flatness values are independent of the propeller rotation frequency (Noullez *et al.* 1997). It may be noted that there is a small dip near zero velocity in the axial velocity component PDF. This occurs because the light sensitivity of the detector decreases when a peak remains on the same pixel for consecutive frames. (This is due to an inefficiency in the shaping amplifiers used for this detector.) As a result, the measurement volume is effectively smaller for trajectories with near-zero velocity, causing a measurement bias. It should be noted that measurement biases depend mostly on the velocity and do not affect acceleration measurements, except to the extent that the acceleration and velocity are correlated.

The scaling of the r.m.s. velocity with propeller rotation frequency is shown in figure 14. The expected linear dependence on the frequency is observed for both components, which is consistent with the assumption that the nature of the large-scale flow is independent of the stirring velocity over the range of Reynolds number studied. The inset shows that the deviation from the linear scaling law does not exceed a few percent. This deviation is most pronounced at low propeller speeds, perhaps indicating that the turbulence is not 'fully developed' at the lower end of the Reynolds number range.

The ratio of the r.m.s. transverse velocity to the r.m.s. axial velocity is shown in figure 15. The ratio varies only a few percent over the full range of propeller speeds,
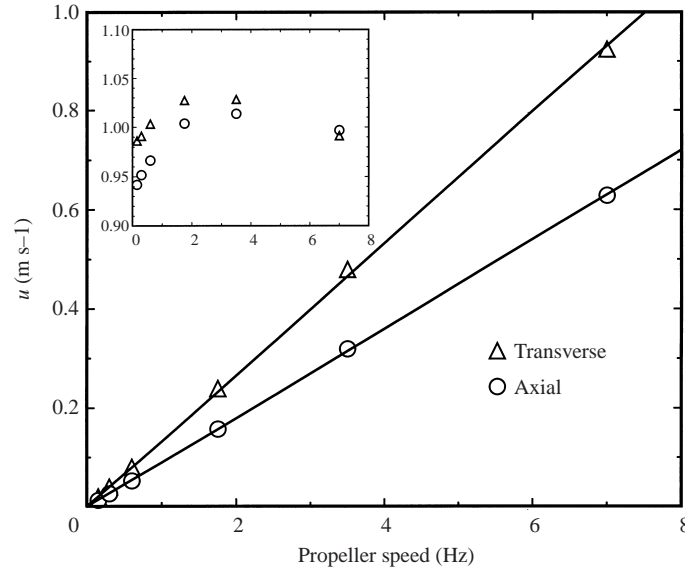
FIGURE 14. The axial and transverse components of the r.m.s. velocity as a function of propeller speed. The lines indicate the best fit to a linear relationship $u_i = k_i f$, with $k_a = 0.090$ for the axial component and $k_t = 0.133$ for the transverse component. The inset shows the r.m.s. velocity components normalized by the linear scaling law.
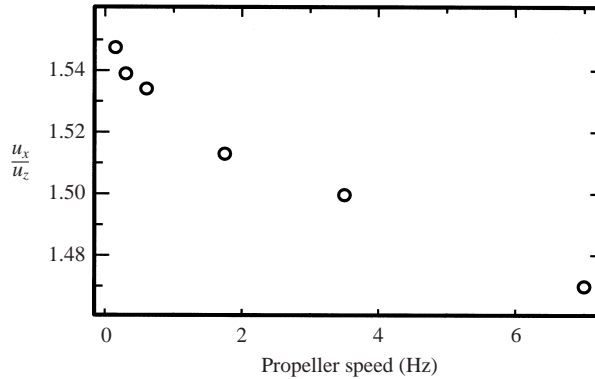

FIGURE 15. The ratio of transverse (x) to axial (z) components of the r.m.s. velocity.

again indicating that the large-scale structure of the flow does not change as the Reynolds number is varied.

3.3. *Energy dissipation*

In order to compare results with Kolmogorov scaling predictions, it is essential to measure the energy dissipation rate ϵ, since all statistical quantities are assumed to depend on this quantity and upon the kinematic viscosity v. The turbulent energy dissipation ϵ is given by

$$\epsilon = 2v\langle s_{ij}s_{ij}\rangle, \tag{3.1}$$

where s_{ij} is the fluctuating rate of strain tensor, defined by

$$s_{ij} = \frac{1}{2}\left(\frac{\partial u_i}{\partial x_j} + \frac{\partial u_j}{\partial x_i}\right), \tag{3.2}$$
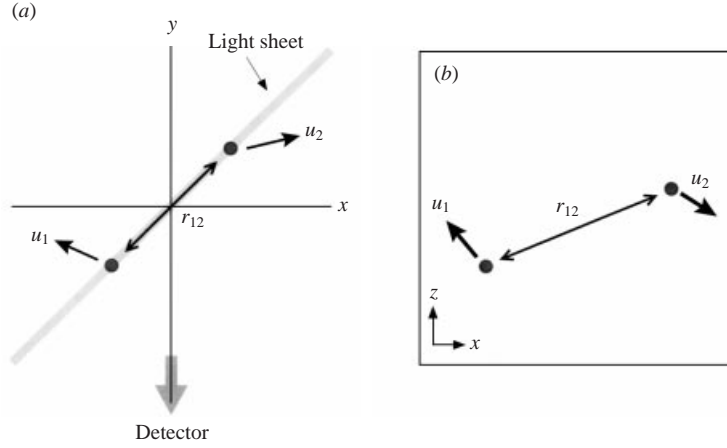
FIGURE 16. (*a*) Experimental setup for dissipation measurements viewed from above (along the axial direction) showing the orientation of the 45° light sheet which illuminates the detection volume. (*b*) Illustration of detector view for dissipation measurements. The detector sees the particle separation and velocity projected on the (x, z)-plane, where z is the axial coordinate.

where $u_i = U_i - \langle U_i \rangle$ is a component of the velocity fluctuation (Pope 2000). Unfortunately Lagrangian particle tracking does not allow us to measure velocity gradients, so a direct measurement of the energy dissipation is not possible.

There are several possible indirect methods for measuring the energy dissipation from particle tracking data (Ott & Mann 2000). The most accessible method requires measurement of second- (or third-) order velocity structure functions. The velocity structure functions are the moments of the velocity differences between two points separated by a fixed difference. The longitudinal and transverse structure functions are calculated from velocity components parallel to and perpendicular to the line separating the two points, respectively. From the second-order structure functions, the energy dissipation can be obtained by comparison with the K41 scaling relations

$$D_{\mathrm{LL}} = C_2(\epsilon r)^{2/3}, \tag{3.3}$$

$$D_{\mathrm{NN}} = \tfrac{4}{3} C_2(\epsilon r)^{2/3}, \tag{3.4}$$

where L and N designate longitudinal and transverse, respectively, and the separation r is assumed to be within the inertial subrange. C_2 is an approximately universal constant that has been determined empirically (Monin & Yaglom 1975; Pope 2000).

All of these structure functions can be calculated from three-dimensional Lagrangian trajectory data by simultaneously measuring the velocities of pairs of particles. However, the particle tracking system used in this experiment is currently not capable of three-dimensional tracking in a volume which would encompass inertial-range particle separations due to power limitations of the argon-ion laser used for illumination. To overcome this, we have developed a technique for measuring the transverse second-order velocity structure function using two-dimensional particle tracking in conjunction with a light sheet.

The structure function measurements are performed using the configuration shown in figure 16. There are several significant differences between this and the standard configuration used for single particle acceleration and velocity measurements. The magnification has been reduced to 2.89, giving a field of view of 17.7 mm ($\geqslant 500\eta$), which allows inertial-range particle separations to be observed. The optical system is

schematically similar to figure 5, except that the beam-splitter is omitted and a single detector is used to measure tracks. The bias of the detector is set so that conjugate peaks are enabled and two-dimensional trajectories can be obtained from the single detector output, as discussed in § 2.1 above. In order to maintain adequate illumination intensity over such a large field of view, the illumination beam is configured as a light sheet approximately 0.1 mm thick and 10 mm wide. The light sheet was created using a standard Galilean telescope to expand the beam to a large TM_{00} mode, then a second cylindrical telescope to compress the horizontal axis and create an elliptical mode. The measurement would be simpler in principle if the light sheet were parallel to the image plane, but in practice it must be oriented at 45° with respect to the optical axis in order to obtain sufficiently strong light scattering from the particles. The data obtained from this configuration consist mostly of short tracks which are created as the particles pass through the light sheet. The depth of the light sheet is chosen so that tracks have sufficient length for an accurate velocity measurement to be made.

Velocity structure functions are measured as a function of r by calculating velocity differences for all coincident pairs of particles and compiling statistics under the condition that the separation distance lies within an adjustable range. Such a pair of particles will appear to the detector as shown in figure 16(b), and it is possible to measure two velocity components for each particle and two components of the particle separation vector. However, as illustrated in figure 16(a), the separation vector does not lie in the same plane as the velocity components. Using the coordinate system defined in figure 16 the coordinates x and z are measured explicitly and we may assume that $y \equiv x$. The velocities are determined by tracking the particle for the short time that it remains within the finite thickness of the light sheet, and gives the projection of the velocity on the imaging plane. We therefore measure the components u_x and u_z, but u_y is unknown.

Using this geometry, it is not possible to measure the longitudinal structure function because it is in general not possible to measure a velocity component along the separation vector. However, it is always possible to measure one of the velocity components perpendicular to the separation vector. To find the measurable transverse velocity component, we make use of the fact that this component must be perpendicular to both the separation vector $\boldsymbol{r}_{12}$ and to the vector normal to the image plane ($\hat{\boldsymbol{y}}$). Such a vector may be constructed by taking the cross product of $\boldsymbol{r}_{12}$ and y. The transverse velocity component is then

$$u_{\perp 2} - u_{\perp 1} = (\boldsymbol{u}_2 - \boldsymbol{u}_1) \cdot (\boldsymbol{r}_{12} \times \hat{\boldsymbol{y}}) / \|\boldsymbol{r}_{12} \times \hat{\boldsymbol{y}}\|, \tag{3.5}$$

where $\boldsymbol{u}_1$ and $\boldsymbol{u}_2$ are the velocities of the two particles. The dot product can be evaluated even though the y-component is unknown because the y-component of $\boldsymbol{r}_{12} \times \hat{\boldsymbol{y}}$ is identically zero.

The structure functions are calculated from the second moment of $(u_{\perp 2} - u_{\perp 1})$ conditional on $\boldsymbol{r}_{12}$,

$$D_{NN}(\bar{r}) = \langle (u_{\perp 2} - u_{\perp 1})^2 | r < \|\boldsymbol{r}_{12}\| < (1+s)r \rangle, \tag{3.6}$$

where the relative bin width s is maintained constant as r is varied and where $\bar{r}$ is the mean value of $\|\boldsymbol{r}_{12}\|$ for all events which satisfy the condition.

Raw data used in the structure function are shown in figure 17(a) and x- and z-coordinate tracks (calculated from primary and conjugate peaks, respectively) are shown in figure 17(b). The matching of x and z tracks is performed using intensity correlations (as described in Appendix A below). The results of the matching are
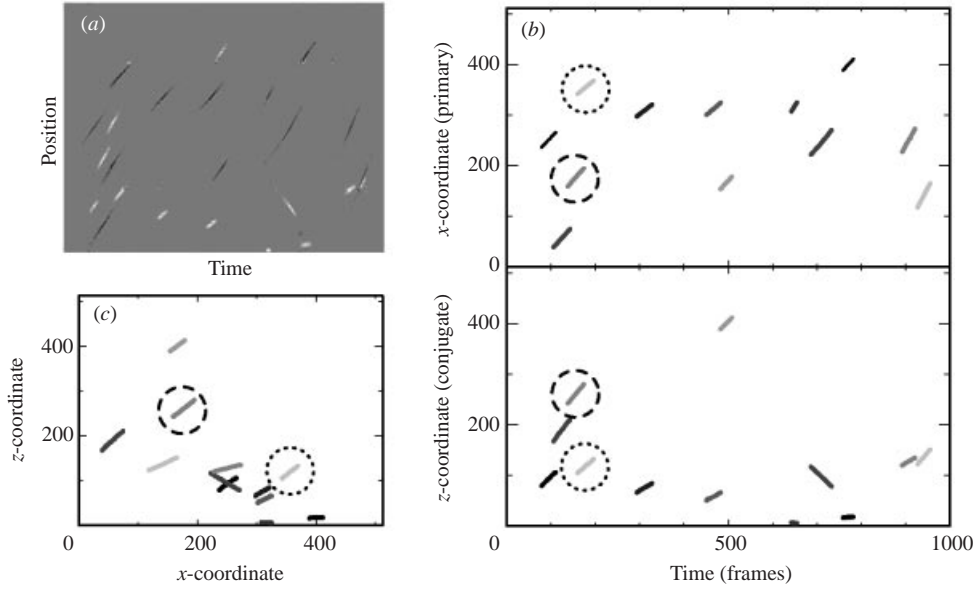
FIGURE 17. (*a*) Raw intensity data, in which dark areas indicate primary (positive) charge and light areas indicate conjugate (negative) charge. (*b*) Position vs. time for x (primary) and z (conjugate) coordinates. (*c*) Reconstruction of x, z trajectories after track matching. The dashed and dotted circles indicate a pair of simultaneous tracks from which velocity differences may be measured.
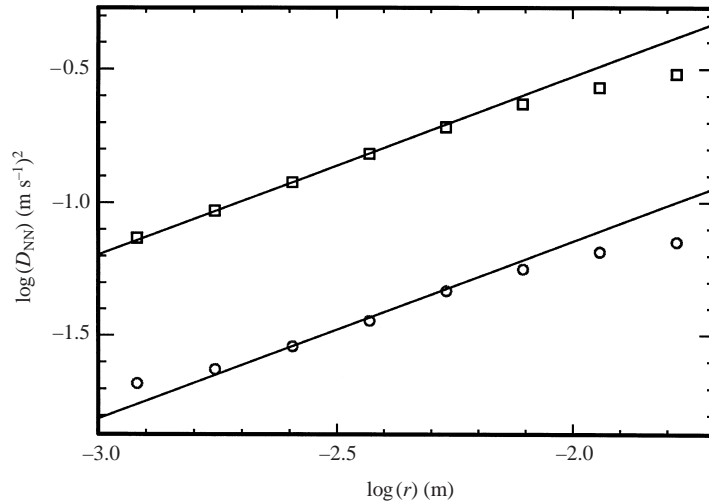

FIGURE 18. Log plot of the scaling of D_{NN} with r. The square symbols indicate data at 5 Hz and the round symbols at 2.5 Hz. The straight lines indicate best fit to $r^{2/3}$, as indicated in table 1.

shown in figure 17(*c*). The scaling of D_{NN} with r is shown in figure 18. Both exhibit the expected $r^{2/3}$ scaling over a substantial range. The scaling range is limited at small r because particles are too close together to be well localized by the light sheet and at large r because their separation is approaching the integral length scale. The energy dissipation rates obtained from the fits in figure 18 are shown in table 1, and are consistent with the expected $\epsilon = \tilde{u}^3/L$ scaling with $L = 7.1$ cm. Once the energy

f (Hz)	$\tilde{u}$ (m s^{-1})	ϵ (m^2 s^{-3})	L (m)
2.5	0.3095	0.406	0.073
5.0	0.6190	3.367	0.070

TABLE 1. Turbulence parameters for dissipation data. The integral length scale L is calculated using $\epsilon = \tilde{u}^3/L$ and $C_2 = 2.13$ (Sreenivasan 1995).

dissipation has been determined, it is possible to calculate the Taylor microscale, $\lambda = (15\nu\tilde{u}^2/\epsilon)^{1/2}$ and the Taylor microscale Reynolds number

$$R_\lambda = \frac{\tilde{u}\lambda}{\nu} = \left(\frac{15\tilde{u}L}{\nu}\right)^{1/2} = \frac{15^{1/2}\epsilon^{1/6}L^{2/3}}{\nu^{1/2}}. \tag{3.7}$$

3.4. *Mean rate of strain*

The optical configuration used for the dissipation measurements is also useful for investigation of the structure of the large-scale flow near the centre of the apparatus. Due to the symmetry at the centre of the flow, the off-diagonal elements of the mean rate of strain tensor $\partial U_i/\partial x_j$ are zero, and the diagonal elements are constrained by symmetry in the transverse plane and the incompressibility condition, $\partial U_i/\partial x_i = 0$ (using the summation convention), so that $\partial U_z/\partial z = -2\partial U_x/\partial x = -2\partial U_y/\partial y$. Measurements at 5.0 Hz and 2.5 Hz show a linear relationship $\partial U_z/\partial z = \tilde{u}/0.0492$ m. This may be compared with a component of the fluctuating strain, which is related to the dissipation in an isotropic flow by $\epsilon = 15\nu(\partial u_z/\partial z)^2$. The ratio of the fluctuating strain to the mean strain is therefore

$$\frac{(\partial U_z/\partial z)}{(\partial u_z/\partial z)} = \frac{(15\nu L)^{1/2}}{0.0492}u^{-1/2} = 0.021u^{-1/2}. \tag{3.8}$$

This implies that at the maximum propeller speed of 7 Hz, the mean strain is about 2% of the fluctuating strain and rises to about 15% of the fluctuating strain at the minimum propeller speed of 0.15 Hz.

4. Results: particle acceleration measurements

The primary subject of this paper is the study of fluid particle accelerations in fully developed turbulence. In contrast to the fluid particle velocity, which is the same quantity that would be measured by a fixed probe at the same location, the particle acceleration is most naturally measured using Lagrangian techniques. The acceleration of a fluid particle $\boldsymbol{a}^+$ corresponds to the substantive derivative of the velocity

$$\boldsymbol{a}^+ \equiv \frac{\partial \boldsymbol{u}}{\partial t} + (\boldsymbol{u} \cdot \nabla)\boldsymbol{u}. \tag{4.1}$$

In order to determine $\boldsymbol{a}^+$ from Eulerian measurements, it would be necessary to know $\partial \boldsymbol{u}/\partial t$ as well $\boldsymbol{u}$ and $\nabla \boldsymbol{u}$ at a point in space (which is possible in DNS but not in experiments). In terms of the fluid particle acceleration, the Navier–Stokes equation is

$$\boldsymbol{a}^+ = -\frac{\nabla P}{\rho} + \nu\nabla^2\boldsymbol{u}, \tag{4.2}$$
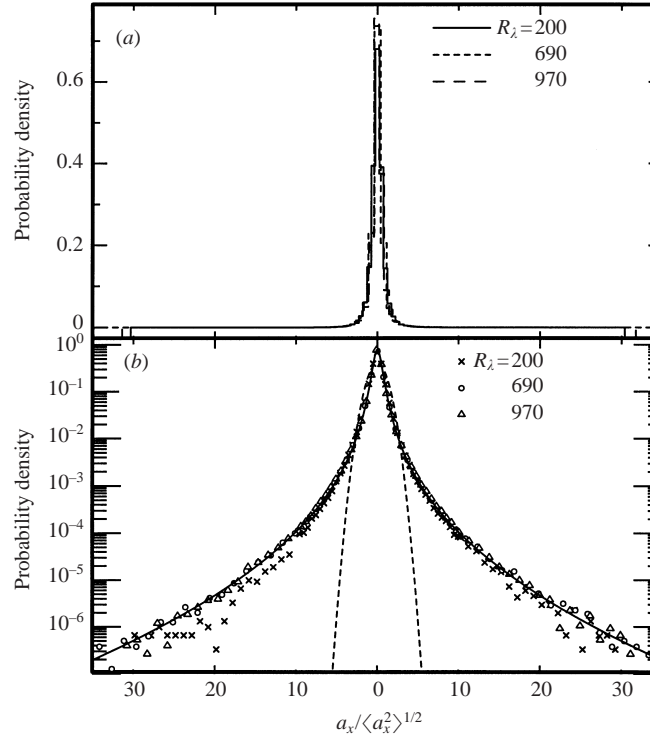
FIGURE 19. The PDF of the transverse (x) component of the acceleration at three values of R_λ plotted on (a) linear and (b) log scale. Each acceleration distribution is measured by parabolic fits over $0.75\tau_\eta$ and is normalized by its standard deviation. The dashed curve is a Gaussian with the same standard deviation and the solid curve is the parameterization defined in equation (4.3).

where P is the pressure and ρ is the fluid density. In fully developed turbulence, the viscous term is small compared with the pressure gradient term, so a measurement of $\boldsymbol{a}^+$ gives information about the pressure gradient, which is difficult to measure experimentally.

Measurements of the acceleration require the lowest possible position error, and were made exclusively from primary charge readout (rather than from the less accurate conjugate charge readout). Accelerations were measured from two-dimensional trajectories recorded in the configuration illustrated in figure 5(a). Accelerations are therefore known in the (x, z)-plane, giving one axial and one transverse component. (Due to symmetry, the statistical properties of the unmeasured y-coordinate are expected to be identical to those of the x-coordinate.)

4.1. *Acceleration distribution*

The PDF of the x (transverse) component of the acceleration is shown on linear and logarithmic scales for several values of R_λ in figure 19. It is found that the distributions have a stretched exponential form for all measured values of R_λ, but that the extension of the tails increases with R_λ. The distributions are plotted for fits to a finite time interval τ_f of $0.75\tau_\eta$. Although there is no qualitative change in the distribution as the fit time is varied over a range $0.5\tau_\eta < \tau_f < 2\tau_\eta$, the moments of the distribution tend to increase as τ_f is reduced. Estimates of the variance and flatness of the acceleration distribution ($\langle a_i^2 \rangle$ and $\langle a_i^4 \rangle / \langle a_i^2 \rangle^2$, respectively) must therefore be
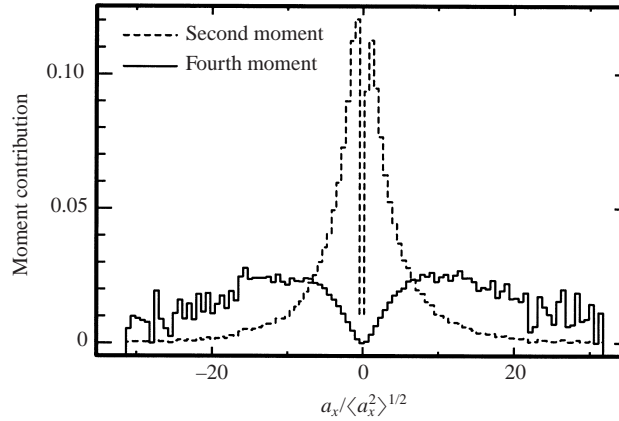
FIGURE 20. The curves show the relative contribution to the second and fourth moments of the transverse acceleration component ($a_x^2 P(a_x)/\langle a_x^2 \rangle$ and $a_x^4 P(a_x)/\langle a_x^4 \rangle$) respectively, as a function of acceleration. $P(a_i)$ is the PDF of the i-component.

obtained by measuring these quantities as a function of τ_f and extrapolating to zero, as will be described in §4.2 below. However, on the basis of figure 19 it is obvious that the tails extend far beyond those of a Gaussian distribution of the same variance and that the flatness of the acceleration is very large (> 40, compared with 3 for a Gaussian). This result is consistent with the large pressure gradient flatness values measured at low Reynolds numbers in DNS (Vedula & Yeung 1999).

The acceleration component PDF may be parameterized by the phenomenological function

$$P(a) = C \exp(-[a^2]/[(1 + |a\beta/\sigma|^\gamma)\sigma^2]), \tag{4.3}$$

where $\beta = 0.539$, $\gamma = 1.588$, $\sigma = 0.508$ and $C = 0.786$ were obtained for the data at $R_\lambda = 970$. It has been shown by Holzer & Siggia (1993) that if the tails of the velocity difference distribution are exponential, then the acceleration PDF should exhibit scaling $P(a) \propto \exp(-a^{1/2})$. This may be compared with the tails of equation (4.3) which have the form $\exp(-|a|^{0.41})$.

Beck (2001a) has also shown that the data may be described by a fit which is derived using Tsallis statistics. Very large amounts of data are required for convergence of the fourth moment since the acceleration PDF has such long tails. Figure 20 shows the contribution to the second and fourth moments as a function of acceleration. Using Tsallis statistics Beck (2001b) argues that the fourth moment should diverge for $R_\lambda \to \infty$. In figure 20, the fourth moment seems to be converging, but it is apparent that even with 5×10^6 acceleration measurements, the convergence is marginal and no definite conclusions about the fourth moment convergence can be drawn from our present data.

The extent to which the anisotropy of the flow affects the acceleration PDF is illustrated in figure 21. The plot shows the PDFs for a_x and a_z at $R_\lambda = 970$. Comparison with figure 13 shows that the acceleration is much less anisotropic than the velocity. The small difference in the variances of a_x and a_z will be discussed below in §4.2.

4.2. *Acceleration variance*

The variance of particle accelerations in a turbulent flow was first predicted on the basis of the 1941 scaling theory of Kolmogorov (1941a, b) by Heisenberg and Yaglom
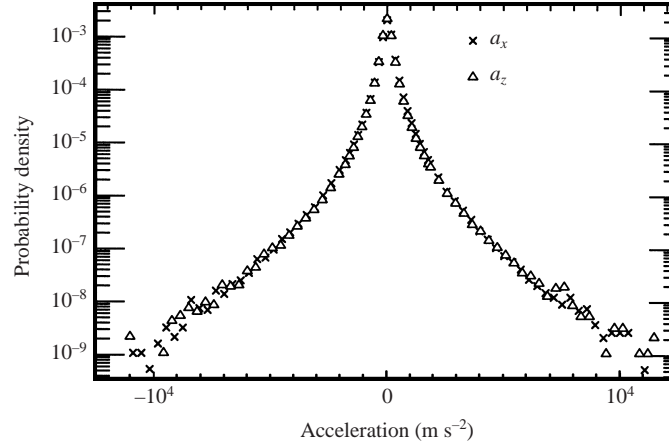
FIGURE 21. Acceleration distributions for transverse (x) and axial (z) components of the particle acceleration for a run at $R_\lambda = 970$. The acceleration was calculated for fits over $1\tau_\eta$. The standard deviations for a_x and a_z are $382\,\mathrm{m\,s^{-2}}$ and $364\,\mathrm{m\,s^{-2}}$ respectively.

(Heisenberg 1948; Yaglom 1949). The variance of the acceleration components is given by

$$\langle a_i a_j \rangle = a_0 \epsilon^{3/2} v^{-1/2} \delta_{ij}, \tag{4.4}$$

where a_0 is predicted to be a universal constant which is approximately 1 in a model assuming Gaussian fluctuations (Heisenberg 1948). The form of this scaling law can be deduced from the assumption that the acceleration is a dissipation-scale quantity, and must be determined only by ϵ and v.

Deviations from the Heisenberg–Yaglom scaling law are expected to arise from turbulent intermittency. Using the refined similarity theory, equation (4.4) is replaced with

$$\langle a_i a_j \rangle = a_0 v^{-1/2} \delta_{ij} \langle \epsilon_r^{3/2} \rangle, \tag{4.5}$$

where ϵ_r, the energy dissipation averaged over a sphere of radius r, has taken the place of the mean energy dissipation, ϵ. Using the log-normal model for the moments of ϵ_r, this yields

$$\langle a_i a_j \rangle \propto (L/\eta)^{3\mu_2/8} \propto R_\lambda^{9\mu_2/16} = R_\lambda^{0.14}, \tag{4.6}$$

where a value of $1/4$ has been used for the intermittency exponent, μ_2. Other models of intermittency have been developed, such as the explicitly Lagrangian model of Borgas (1993), which predicts $a_0 \propto R_\lambda^{0.135}$.

Direct numerical simulation of turbulence has shown that at low Reynolds number $a_0 \propto R_\lambda^{1/2}$ (or $\epsilon^{1/12}$, using equation (3.8) and assuming constant L and v). This is equivalent to an overall scaling of the acceleration variance with $\epsilon^{19/12}$, which is a relatively small deviation from the Heisenberg–Yaglom prediction of $\epsilon^{3/2}$.

In principle, the acceleration variance may be calculated by taking the second moment of the distributions shown in figure 19. However, in order to calculate the particle accelerations the track must be fit over a finite time, and the moments of the distribution depend on this fit time interval. The issue is illustrated in figure 22, which shows a typical particle trajectory. The raw trajectory appears to be straight, but when the mean velocity is subtracted off, the particle is seen to be undergoing a small
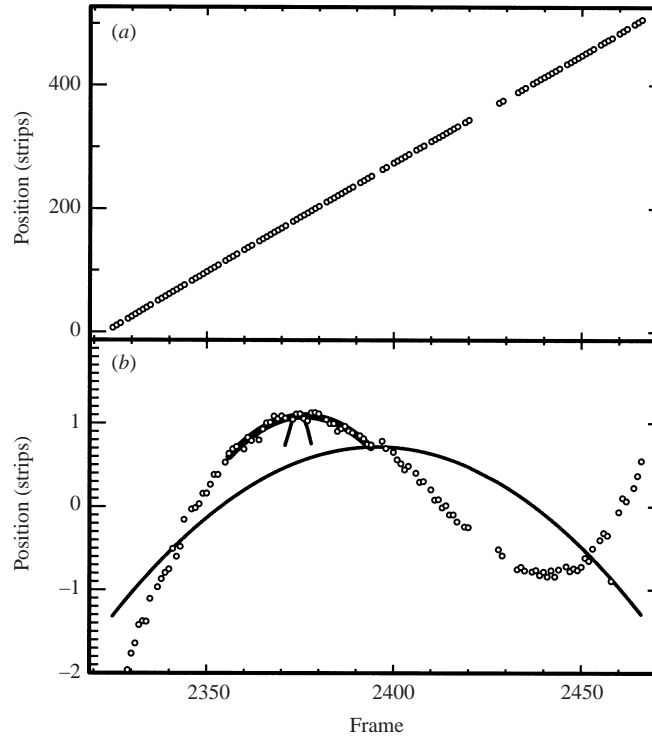
FIGURE 22. (*a*) An apparently straight particle trajectory recorded at $R_\lambda = 970$. The duration of the track is approximately 150 frames, 2 ms, or $7\tau_\eta$. (*b*) The same trajectory after the mean velocity has been subtracted off. The three lines show parabolic fits over intervals of 150, 40 and 5 frames.

time-varying acceleration, which causes it to deviate from a straight trajectory by a distance corresponding to a few strips on the detector. The acceleration of this track is approximately $90 \, \mathrm{m \, s^{-2}}$, which is about one quarter of the r.m.s. acceleration – a typical value. Clearly the correct acceleration will be measured from this track only if a parabolic fit is made over an appropriate time interval. The fit over 150 frames does not conform to the trajectory and underestimates the acceleration. The fit over 5 frames conforms to the position measurement errors and dramatically overestimates the acceleration. The fit over 40 frames ($1.8\tau_\eta$) appears to conform to this particular trajectory.

Ideally, we would like to fix the fit interval at a value where the noise is adequately averaged and yet the parabolic fits are able to conform to all of the particle trajectories. Figure 23 shows the normalized variance of the acceleration distribution as a function of the fit interval τ_f, and demonstrates that no value of τ_f exists which satisfies this criterion, since there is no range of τ_f where the acceleration variance is independent of τ_f. For $\tau_\eta \leqslant \tau_f \leqslant 9\tau_\eta$ there is an approximately exponential dependence of the acceleration variance on τ_f which is due to the failure of the fits to conform to the true particle trajectories. For $\tau_f < \tau_\eta$ the acceleration variance rises dramatically with a $\approx \tau_f^{-5}$ power law dependence. This is the τ_f dependence which would be obtained from uncorrelated Gaussian distributed noise, and evidently arises from the position measurement error.

The fact that the onset of position uncertainty occurs at a value of τ_f where the fits fail to fully conform to the turbulent trajectories indicates that the frequency spectra
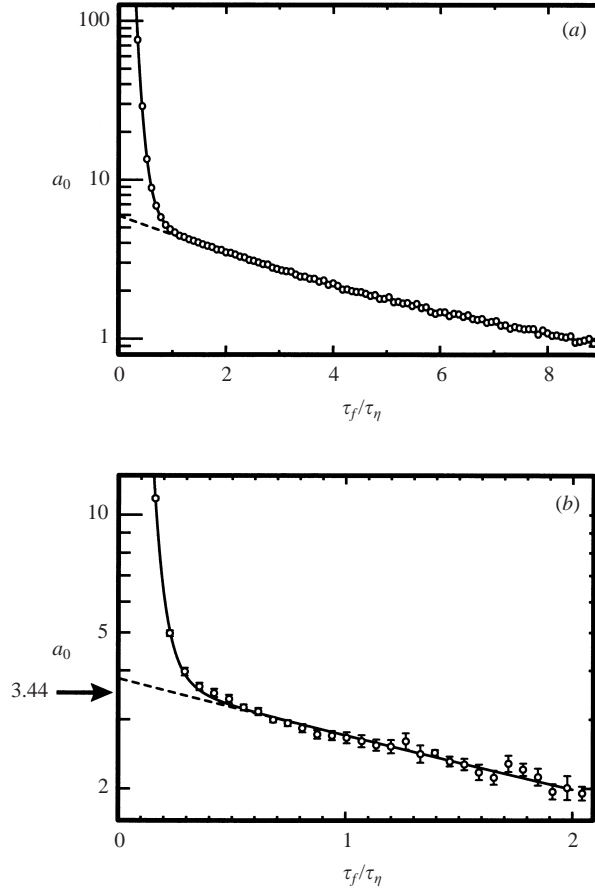
FIGURE 23. Normalized acceleration variance (a_0) of the x-component as a function of fit interval normalized by the Kolmogorov time (τ_f/τ_η). (a) The circles represent data taken at $R_\lambda = 970$, the solid line indicates the best fit of the function in equation (4.7), and the dashed line shows the exponential term. (b) The squares represent trajectories obtained from direct numerical simulation of turbulence at $R_\lambda = 240$ (Vedula & Yeung 1999). The solid line indicates the best fit of the function in equation (4.7), and the dashed line shows the exponential term. The value of a_0 obtained from direct calculation from the simulation is 3.44. The extrapolation technique overestimates this value by approximately 10%.

of these two processes are not distinct, but overlap. Therefore it is not possible to distinguish between these two contributions on any given track. However, we can separate the two effects by making use of the fact that the two contributions to the acceleration variance have very different scaling with τ_f. The procedure we use is to fit the data (shown in figure 23a) of the measured a_0 (the normalized acceleration variance) vs. fit time to the function

$$f(\tau) = A\tau^B + C\exp(D\tau + E\tau^2), \qquad (4.7)$$

where A, B, C, D and E are fit parameters. The power law term represents the contribution from the position noise and the exponential term represents the contribution of the turbulence to the acceleration variance. (The τ^2 term is added to model the slight deviation from exponential dependence observed at large τ_f.) The best estimate of a_0 is then obtained by evaluating the exponential term in the limit where $\tau_f \to 0$,

f (Hz)	$\tilde{u}$ (m s^{-1})	τ_s (ms)	ϵ (m^2 s^{-3})	τ_η (ms)	η (μm)	R_λ	Re	Δt (μs)	$\tau_\eta/\Delta t$	τ_s/τ_η
0.15	0.0186	107	9.01×10^{-5}	105	322	140	1340	205	512	1.02
0.30	0.0371	53.9	7.21×10^{-4}	37.0	191	200	2690	150	257	1.46
0.41	0.0509	39.7	1.85×10^{-3}	23.1	151	235	3680	116	200	1.72
0.60	0.0743	26.9	5.77×10^{-3}	13.1	114	285	5380	74.9	175	2.05
1.75	0.217	9.22	0.143	2.63	51.0	485	15 700	25.9	102	3.50
3.5	0.433	4.62	1.14	0.929	30.3	690	31 400	14.3	65	5.27
7.0	0.867	2.31	9.16	0.329	18.0	970	62 700	14.3	23	6.99

TABLE 2. Turbulence parameters for acceleration data with $v = 9.89 \times 10^{-7}$ m^2 s^{-1} (water at 20.6°). f is the propeller rotation frequency and Δt is the strip detector frame period. $\tilde{u} = ((\bar{u}_x^2 + \bar{u}_y^2 + \bar{u}_z^2)/3)^{1/2}$ is the r.m.s. velocity. The sweeping time τ_s is calculated from $\tilde{u}$ and the 2.00 mm field of view of the detector. The energy dissipation is calculated from $\epsilon = u^3/L$ with $L = 0.071$ m, as discussed in §3.3. The Taylor microscale Reynolds number R_λ is calculated from equation (3.7) and the classical Reynolds number Re is defined by $Re = R_\lambda^2/15$.

so that $a_0 = C$. It is known that this extrapolation must overestimate the value of a_0 because the slope of the a_0 vs. τ_f curve must go to zero at $\tau_f = 0$ since the tracks are differentiable.

To determine how the extrapolation to zero fit time is related to the true acceleration variance, we used a simulation of the detection process. The simulation is based on three-dimensional particle trajectory data from Vedula & Yeung's (1999) DNS simulation at $R_\lambda = 240$, which is known to have $a_0 = 3.44$. These trajectories were dimensionalized using the viscosity of water and the rate of energy dissipation which would be needed to produce the same Reynolds number in our apparatus. These scaled trajectories were used as input to a computer model which simulated the illumination of the particles and the imaging of our measurement volume onto the strip detectors, including diffraction and defocusing of the imaging system. The computer model also simulated charge collection by the strip detector, including correlated and uncorrelated noise, charge diffusion, and inoperative pixels. The intensities produced by the simulation were then run through the real-time thresholding and compression algorithms used in the experiment, and were subsequently processed by the same data processing algorithms as used for actual experimental data.

The measurement of a_0 as a function of normalized fit interval for the simulation data is shown in figure 23(b) (which may be compared with figure 23a). The exponential dependence on τ_f is reproduced for large τ_f, as is the power law dependence for small τ_f. The extrapolation for $\tau_f \to 0$ gives a value of 3.80. This value is 10% higher than the value of 3.44 which was measured directly from the simulation (Vedula & Yeung 1999).

In order to correct for the systematic overestimation of a_0 by our analysis technique we have rescaled all normalized acceleration variance measurements presented in this paper by 10%. For R_λ other than 240, this correction depends on the assumption that the dependence of the measured value of a_0 on (τ_f/τ_η) has a universal form for small τ_f.

The procedure described above was used to calculate the acceleration variance for the x- and z-components of the acceleration for all values of the Reynolds number. Figures 24(a) and 24(b) show a_0 as a function of τ_f for the x- and z-components of the acceleration, respectively. The maximum value of τ_f for which the acceleration
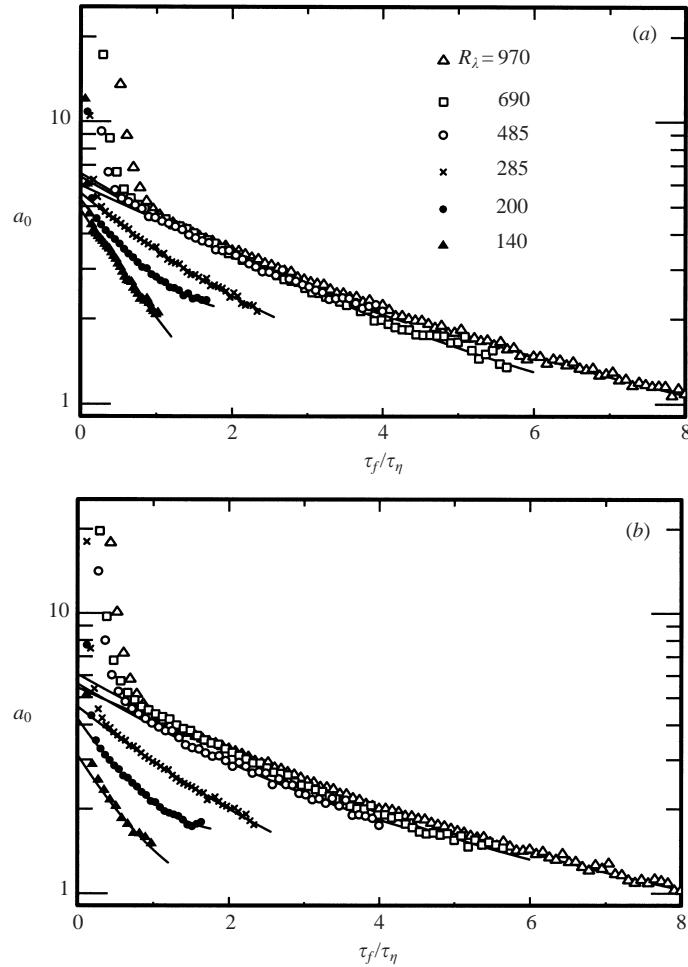
FIGURE 24. Plots of the normalized variance of an acceleration component, a_0, as a function of normalized fit time τ_f/τ_η for the full range of Reynolds number. The lines indicate the exponential term $C \exp D\tau + E\tau^2$ from the best fit for each curve. The tabulated values of a_0 are derived from the extrapolation of this term to $\tau = 0$. (*a*) *x*-component, (*b*) *z*-component.

variance can be calculated is determined by the length of time the particles remain in view. This is estimated using the sweeping time τ_s, which is the length of time a particle moving at the r.m.s. velocity would remain in the detection volume (tabulated in table 2). For purposes of fitting to equation (4.7) the range of each a_0 curve in figure 24 was limited at low τ_f to the value where the power law term contributes an order of magnitude more than the exponential term, and at high τ_f to $1.15\tau_s$.

Certain conclusions may be drawn from figure 24. The curves for the three high-Reynolds-number runs collapse onto a single curve, indicating that the scaling of the acceleration with time is well approximated by K41 scaling. At low Reynolds numbers, the slopes of the curves and their extrapolations to $\tau_f = 0$ fail to collapse, indicating that K41 scaling has broken down. However, the interpretation is somewhat more complex because the measurement process brings an additional time scale into play. As the Reynolds number is reduced, the ratio of the residence time of the particles τ_s to the Kolmogorov time τ_η becomes smaller. If there is any correlation between
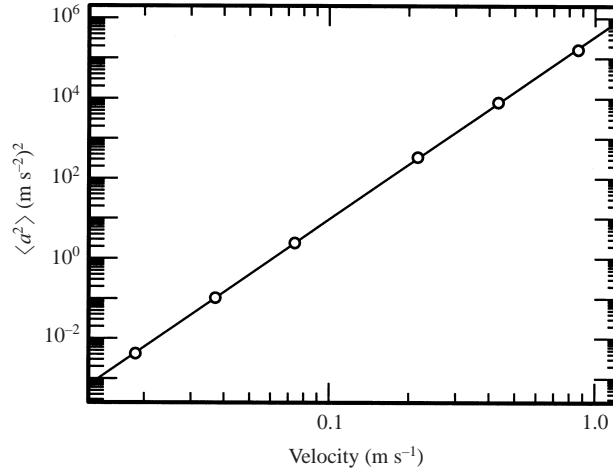
FIGURE 25. The variance of the acceleration plotted as a function of $\tilde{u}$. The straight line is the best fit of $\tilde{u}^{9/2}$ ($\epsilon^{3/2}$ with $\epsilon = \tilde{u}^3/L$) to the data.

f (Hz)	R_λ	$(a_0)_x$	$(a_0)_z$	$(a_0)_x/(a_0)_z$
0.15	140	4.60 ± 0.40	3.01 ± 0.27	1.53
0.30	200	4.99 ± 0.28	4.07 ± 0.48	1.23
0.60	285	5.26 ± 0.28	4.49 ± 0.70	1.17
1.75	485	6.01 ± 0.33	5.12 ± 0.23	1.17
3.50	690	6.18 ± 0.42	5.85 ± 0.27	1.06
7.00	970	5.61 ± 0.35	5.23 ± 0.34	1.07

TABLE 3. a_0 as a function of Reynolds number for transverse and axial acceleration.

residence time and acceleration, then this implies that similarity cannot be achieved by rescaling the time axis with τ_η. By varying the size of the measurement volume (and hence the sweeping time τ_s) we have observed that the slope of the a_0 vs. τ_f curve has some dependence on the finite size of the measurement volume, although the extrapolation to $\tau_f = 0$ is found to be independent of the measurement volume. For this reason the $\tau_f \to 0$ extrapolation is a more reliable measure of a_0 than its value at any finite τ_f.

The variance of the (unnormalized) x-component of the acceleration is shown as a function of the r.m.s. velocity $\tilde{u}$ in figure 25. It is found that the predicted scaling

$$\langle a_x^2 \rangle = \frac{a_0 \tilde{u}^{9/2}}{L^{3/2} \nu^{1/2}} \tag{4.8}$$

(from equation (4.4), using $\epsilon = \tilde{u}^3/L$), is observed over nearly 7 orders of magnitude in acceleration variance, or nearly 2 orders of magnitude in velocity variance. The scaling of a_0 with R_λ is plotted in figure 26 and tabulated in table 3. In this plot, a constant value of a_0 would indicate Heisenberg–Yaglom scaling. As R_λ is decreased below 500 the value of a_0 decreases substantially showing a small but significant departure from universal scaling. The dependence of a_0 on R_λ in this regime seems to be qualitatively consistent with DNS results. It is not surprising that DNS and experimental results do not match exactly at small Reynolds number, since in this
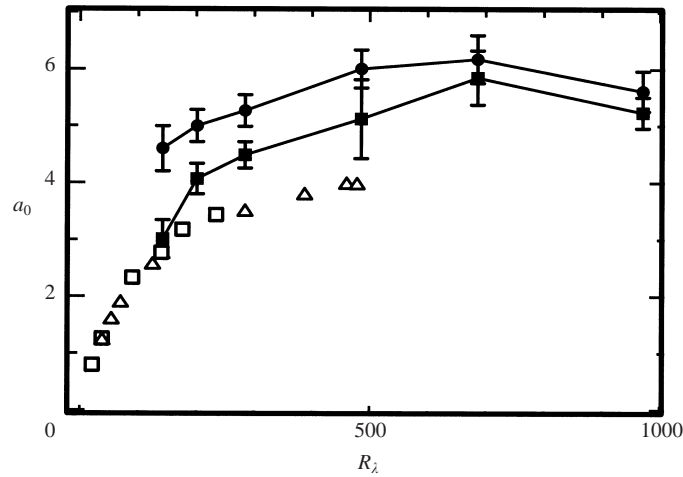
FIGURE 26. The Kolmogorov constant a_0 calculated for transverse (filled circles) and axial (filled squares) components of the acceleration, as a function of Reynolds number. These values have a 10% correction applied to them as discussed in § 4.2. Values obtained from direct numerical simulation of turbulence by Vedula & Yeung (1999), and by Gotoh & Fukayama (2001) are also shown by open squares and open triangles, respectively.

range the acceleration is coupled to the large scales of the flow. The DNS results were obtained for isotropic turbulence with periodic boundary conditions, which differs markedly from the anisotropically forced turbulence between counter-rotating disks used in the experiment. At high Reynolds number ($R_\lambda \geqslant 500$) a_0 appears to be independent of R_λ, which is consistent with Heisenberg–Yaglom scaling. Due to experimental uncertainties, very weak deviations such as the $R_\lambda^{0.135}$ prediction of the Borgas multi-fractal model cannot be ruled out by these data.

It has been shown that the mean-squared pressure gradient in a turbulent flow – and therefore the mean-squared acceleration and a_0 – is closely related to the fourth-order velocity structure functions and to the inertial-range flatness factor (Hill & Wilczak 1995). This would indicate that the a_0 vs. R_λ curve in figure 26 could be compared with the flatness factor (F) vs. R_λ curve reported by Belin *et al.* (1997) in another experiment involving a flow between counter-rotating disks. Some similarity is evident, despite the fact that the flow configurations are quite different (Hill 2001, 2002).

It is also evident that larger a_0 values are obtained for the transverse component than for the axial component of the acceleration, and that the level of anisotropy decreases as the Reynolds number is increased. The anisotropy of the acceleration variance is best illustrated by calculating the ratio $(a_0)_x/(a_0)_z$ as a function of R_λ, as shown in figure 27. At the lowest Reynolds number of 140, $(a_0)_x/(a_0)_y = 1.52$, indicating that the ratio of the standard deviations of the acceleration components is 1.23. As the Reynolds number is increased to 970, the level of anisotropy decreases to a very small value. This observation is consistent with recent experimental results which indicate that anisotropy persists to high Reynolds numbers (Kurien & Sreenivasan 2000; Shen & Warhaft 2000).

It is also informative to compare figure 27 with the inset to figure 14, which shows the ratio of the standard deviations of the velocity components. On the one hand, the particle velocities are associated mainly with the large scales and the level of anisotropy is large and independent of Reynolds number, as expected. On the other
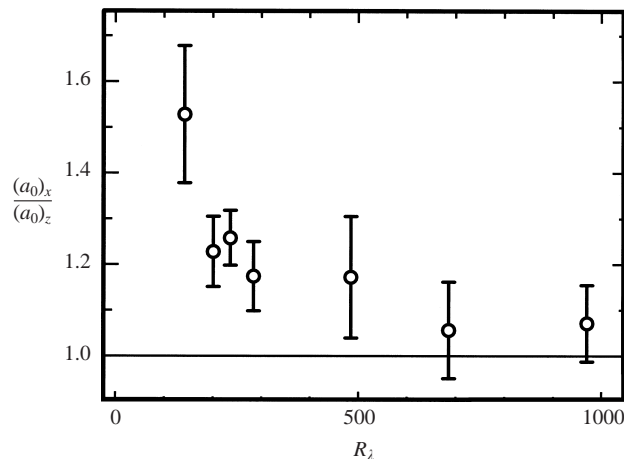
FIGURE 27. The ratio of a_0 calculated for transverse (x) and axial (z) components of the acceleration as a function of Reynolds number.

hand, the particle accelerations come mainly from the dissipation-range scales. As expected, the level of anisotropy for the acceleration is smaller than for the velocity, and decreases as the Reynolds number is increased.

4.3. *Acceleration flatness*

Even though the convergence of the fourth moment is unclear (§4.1, Beck 2001*b*), it is interesting to quantify the degree of intermittency of the acceleration by calculating the acceleration flatness ($\langle a_i^4 \rangle / \langle a_i^2 \rangle^2$) as a function of Reynolds number. In this case, one encounters the same difficulty as for the variance: the flatness varies as a function of the interval over which the acceleration is calculated. One must also confront the added difficulty that the tails of the acceleration distribution are so long that prohibitively large data samples would be needed to definitively converge the fourth moment, as illustrated in figure 20 above. In view of figure 20, it seems possible that the unconverged tails of the acceleration distribution could make substantial contributions to the fourth moment. In addition, the ability of the tracer particles to fully follow rare violent events which contribute most to the flatness has not been fully established. Therefore, we can only set lower bounds on the flatness.

The flatness for the transverse component of the acceleration is shown as a function of fit time in figure 28. An increasing trend is evident as τ_f decreases, but the dependence on τ_f is more difficult to define than in the analogous curves for the acceleration variance (figure 24). We have not found it possible to make a formal extrapolation for $\tau_f \rightarrow 0$ in this case, but by tabulating the flatness at a value of τ_f slightly above the onset of power-law position uncertainty we can compile a plot of lower bounds on the acceleration flatness, shown in figure 29. The flatness is found to be at least 25 at the lowest Reynolds numbers studied and the lower bound increases to approximately 60 as the Reynolds number is increased.

These large flatness values indicate that the acceleration is more intermittent than the other small-scale quantities in turbulence. For example, at $R_\lambda = 200$, the longitudinal velocity derivative flatness is 6.0 (Van Atta & Antonia 1980), and the scalar gradient flatness is 17 (Shen & Warhaft 2000), while the acceleration flatness in both experiments and simulation (Vedula & Yeung 1999) is approximately 30.
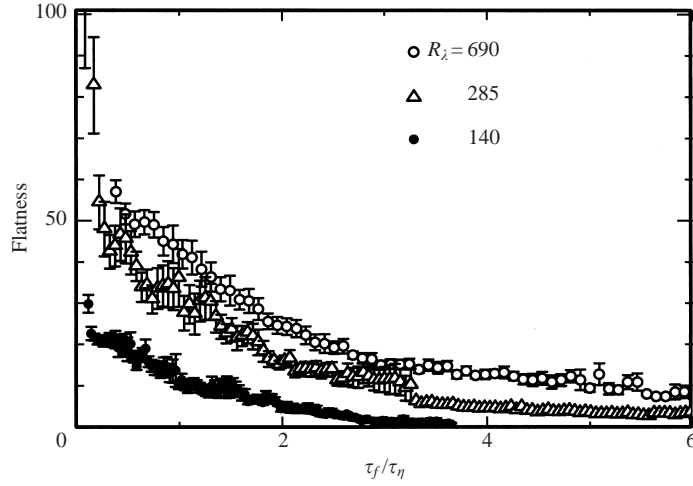
FIGURE 28. Flatness of the transverse component of the acceleration as a function of fit interval τ_f.
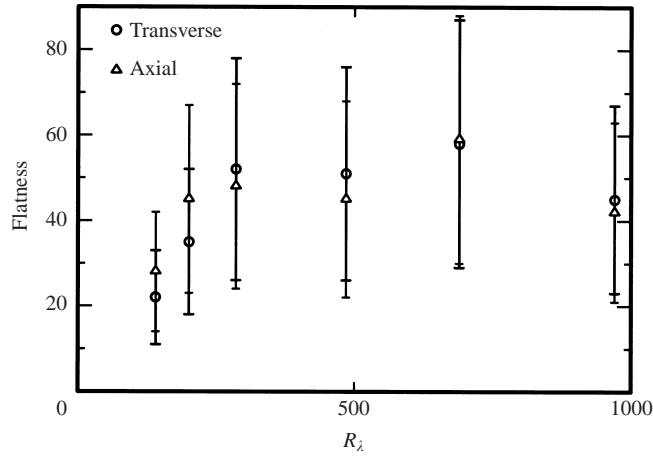
FIGURE 29. Lower bound on the flatness of the transverse and axial components of the acceleration as a function of R_λ. The error bars indicates an estimated uncertainty due to the inability to extrapolate τ_f to zero, but do not reflect uncertainty in the convergence of the fourth moment.

4.4. *Acceleration correlations*

Having measured the acceleration as a function of time for the particle tracks, in principle it is straightforward to evaluate the acceleration autocovariance

$$c_{a^+}(\tau) = \langle a_i^+(t)a_i^+(t+\tau)\rangle \tag{4.9}$$

and the acceleration autocorrelation function

$$C_{a^+}(\tau) = \frac{\langle a_i^+(t)a_i^+(t+\tau)\rangle}{(\langle a_i^+(t)^2\rangle\langle a_i^+(t+\tau)^2\rangle)^{1/2}}, \tag{4.10}$$

where $a_i^+(t)$ is the acceleration component along a particle trajectory and $\langle\ \rangle$ denotes averaging over t for an ensemble of tracks. Due to measurement biases a naive application of equations (4.9) and (4.10) is not appropriate.

The autocorrelation data were compiled using the same trajectories as were used
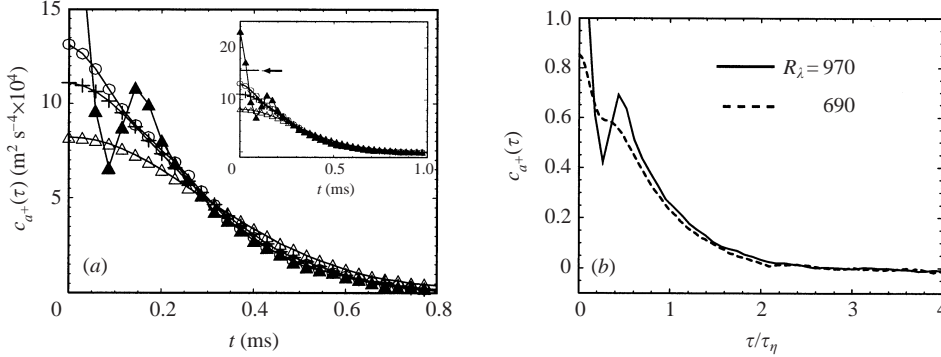
FIGURE 30. (*a*) The acceleration autocovariance is shown for data at R_λ of 970. The accelerations are calculated by direct differencing of trajectories which have been smoothed with a Gaussian kernel with different standard deviations, σ_k: solid triangles $\sigma_k = 0.26\tau_\eta$, open circles $\sigma_k = 0.43\tau_\eta$, plus signs $\sigma_k = 0.60\tau_\eta$, open triangles $\sigma_k = 1\tau_\eta$. The inset shows a zoomed-out view of the figure in which the acceleration variance that was determined in § 4.2 is marked with an arrow. (*b*) The acceleration autocorrelation at $R_\lambda = 690$ and $R_\lambda = 970$ is shown for $\sigma_k = 0.15\tau_\eta$ and $\sigma_k = 0.26\tau_\eta$ respectively. The time axis has been scaled by the Kolmogorov time τ_η.

for the study of the acceleration moments. This presents some difficulty because of the small size of the measurement volume, i.e. the lengths of the tracks are of order a few τ_η. The variances $\langle a_i^+(t)^2 \rangle$ and $\langle a_i^+(t+\tau)^2 \rangle$ are compiled from different data samples and differ slightly, particularly at large τ.

In addition, particles with large accelerations are less likely to remain in view than particles with small accelerations. The autocorrelation function $c_{a^+}(t)$ differs depending on whether all the tracks or only tracks which are at least $\tau_{\max}$ long are used.

Here, the accelerations were determined by direct differencing of trajectories which have been smoothed by a Gaussian kernel with standard deviation σ_k, hereafter referred to as the kernel width. This is similar to using a parabolic fit as in § 4.2 but is more tractable for this calculation. Figure 23 shows that $c_{a^+}(0)$ at large σ_k is overestimated and at small σ_k is underestimated and the true value can only be found by an extrapolation back to $\sigma_k = 0$. This makes the normalization of $c_{a^+}(t)$ to obtain $C_{a^+}(t)$ as in equation (4.10) inaccurate. Nevertheless, it is still possible to measure the autocovariance and autocorrelation for $\tau > 0$.

In order to correct for biasing errors and make a sensible normalization we calculate

$$\tilde{c}_{a^+}(\tau) = \frac{\langle a_i^+(t)a_i^+(t+\tau) \rangle_{t\&\tau}}{(\langle a_i^+(t)^2 \rangle_{t\&\tau} \langle a_i^+(t+\tau)^2 \rangle)_{t\&\tau}^{1/2}} \langle a_i^+(t)^2 \rangle_t, \tag{4.11}$$

$$\tilde{C}_{a^+}(\tau) = \frac{\tilde{c}_{a^+}(\tau)}{a_0 v^{-1/2} \epsilon^{3/2}}; \tag{4.12}$$

$\langle\ \rangle_{t\&\tau}$ indicates that only measurements of acceleration where a measurement at both t and $t+\tau$ existed on the given particle track were averaged over; $\langle\ \rangle_t$ indicates that all measurements of acceleration were averaged over.

Figure 30(*a*) shows $\tilde{c}_{a^+}(\tau)$ for $R_\lambda = 970$ at $\sigma_k = 0.26\tau_\eta$, $0.43\tau_\eta$, $0.60\tau_\eta$ and $1.0\tau_\eta$. For small kernel widths, the oscillation can be attributed to the convolution with the Gaussian kernel (N. Mordant 2002, private communication). For sufficiently large τ,

all of the curves collapse for $\sigma_k < 1\tau_\eta$. This shows that at sufficiently large τ the true shape of the autocovariance is measured.

Figure 30(b) shows $\tilde{C}_{a^+}(\tau)$ for R_λ of 970 and 690. The time axis is scaled by the Kolmogorov time and the data collapse between the two Reynolds numbers shows that Kolmogorov scaling is observed. In order to compare our curves to those of the available direct numerical simulations, we determine the exponential decay time $\tau_{1/e}$, $C_{a^+}(\tau_{1/e}) = 1/e$. Although Yeung & Pope (1989) specify the zero crossing τ_0 ($C_{a^+}\tau_0 = 0$), we find that $\tau_{1/e}$ is a more appropriate choice in our case. At this point the statistics are better and less prone to biasing errors due to the small measurement volume. The curve at the zero crossing has a shallow slope so small deviations in it can cause large deviations in the zero crossing. We find that $\tau_{1/e} = (0.73 \pm 0.05)\tau_\eta$ for $R_\lambda = 690$ and $\tau_{1/e} = (0.80 \pm 0.05)\tau_\eta$ for $R_\lambda = 970$. Measurements from figure 7 in Yeung & Pope (1989) give $\tau_{1/e} = 1.3 \pm 0.1$ for direct numerical simulations at $R_\lambda = 93$ which is 60% larger than the experimental value.

5. Effect of finite particle size on particle accelerations

An important question which must be considered is the extent to which the polystyrene tracer particles are equivalent to ideal fluid particles. In order to address this question, we have repeated our acceleration measurements using tracer particles with a range of particle diameters and fluid densities. Not only are these measurements essential to validate the Lagrangian measurements, but the data for large particle sizes offer a new perspective on the motion of finite size particles in turbulence.

Phenomenologically, we can identify two mechanisms by which a discrepancy between statistics of tracer particle trajectories and fluid particle trajectories could arise. (i) It is possible that the tracer particle's density is different from that of the fluid, so that it experiences an acceleration that is different from the acceleration that would be experienced by a fluid particle at the same location. We call this the density-dependent effect. (ii) It is possible that the tracer particle's size is large enough that the unperturbed flow would change significantly over the volume of the particle. Since this effect remains even when the tracers are density matched, we call this the density-independent effect. The dimensionless numbers that measure these effects are the ratio of the particle to fluid density, ρ_p/ρ_f, and the ratio of the particle diameter to the smallest length scale in the flow, d/η. A commonly used parameter is the ratio of the Stokes time ($d^2\rho_p/\nu\rho_f$) to the Kolmogorov time (η^2/ν) which is the combination of the size and density parameters.

Particle motion in fluid flows has been extensively studied both as a fundamental fluid dynamics topic (Basset 1888; Corrsin & Lumley 1956; Maxey & Riley 1983) and in order to validate measurement techniques that rely on tracer particles (Buchave *et al.* 1979). Most of the work in this area has focused on the dynamics of particles when the density-independent effect is negligible. Not only is this regime amenable to exact theoretical modelling, but it also is a good approximation for the tracers used in many particle image velocimetry and laser Doppler anemometry experiments. In those experiments, it is desirable to have the spacing between particles less than or equal to the size of the smallest flow structures, so the particle size must be much smaller than the smallest structures.

In order to determine the effects of finite particle size on the acceleration measurements, we repeated the measurements at $R_\lambda = 970$ using particles of diameters between $26\,\mu m$ and $450\,\mu m$ (1.44η and 26η). The Stokes times for these particles ranges from $0.67\,ms$ to $216\,ms$, which should be compared to the Kolmogorov time of
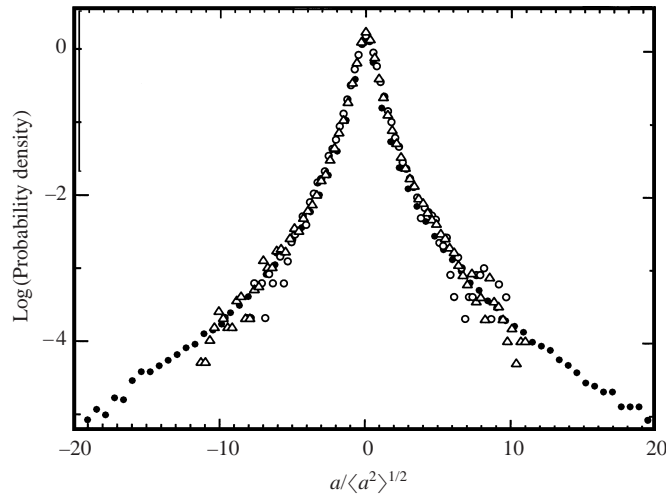
FIGURE 31. PDF of the acceleration for different particle sizes and fluid densities at $R_\lambda = 970$ normalized by the r.m.s. acceleration. Out to 10 standard deviations the shape of the curve is not strongly affected. ●, 50 μm diameter, $\rho_{\text{eff}} = 1.06$, $\langle a^2 \rangle^{1/2} = 0.015\,\text{m s}^{-2}$. ○, 450 μm diameter, $\rho_{\text{eff}} = 1.06$, $\langle a^2 \rangle^{1/2} = 0.005\,\text{m s}^{-2}$. △, 450 μm diameter, $\rho_{\text{eff}} = 0.96$, $\langle a^2 \rangle^{1/2} = 0.006\,\text{m s}^{-2}$.
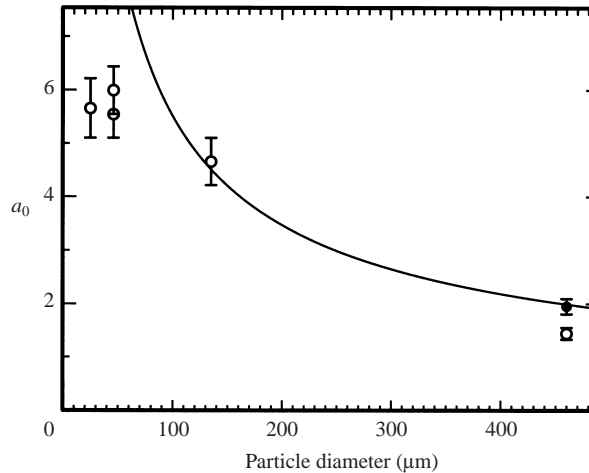

FIGURE 32. Normalized acceleration variance (a_0) as a function of particle diameter at $R_\lambda = 970$. Open circles with error bars are for particles of relative density 1.06. The solid circle with error bars is for particles of relative density 1.0. The Kolmogorov length is 18 μm and the relative density is defined as $\rho_{\text{eff}} = \rho_{\text{particle}} / \rho_{\text{fluid}}$. The solid line shows $d^{-2/3}$ scaling.

0.32 ms. We also measured the acceleration of 450 μm particles in NaCl solutions with densities between $1.00\,\text{g cm}^{-3}$ and $1.11\,\text{g cm}^{-3}$. Since the particle density is $1.06\,\text{g cm}^{-3}$, this range of densities encompasses both negative and positive particle buoyancy. Figure 31 shows the PDF of the acceleration for different particle sizes and fluid densities. Out to 10 standard deviations, the shape of the distribution is not strongly affected by particle size.

In figure 32, the measured Kolmogorov constant a_0 is shown as a function of particle size for acceleration data taken with pure water at $R_\lambda = 970$. A 70% decrease
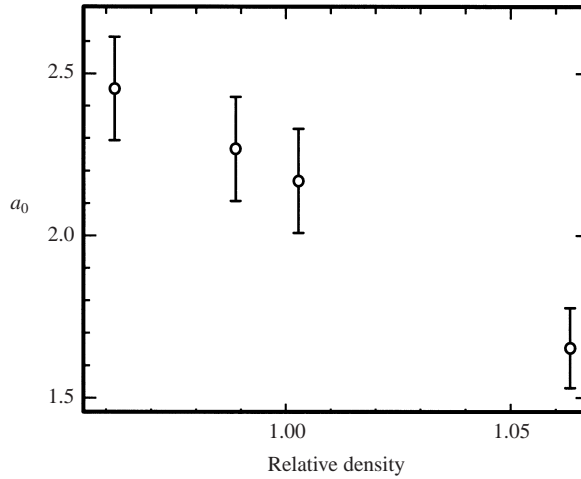
FIGURE 33. a_0 (normalized acceleration variance) as a function of relative particle density for 450 μm particles at $R_\lambda = 970$.

is seen in the measured acceleration variance between the smallest and largest particles used.

The dependence of the particle acceleration on the density mismatch is shown in figure 33, where a_0 is plotted as a function of relative density ($\rho_{\mathrm{eff}} = \rho_{\mathrm{particle}}/\rho_{\mathrm{fluid}}$) for 450 μm diameter particles at $R_\lambda = 970$. In this case, the density of the fluid is varied by the addition of NaCl, and the values of a_0 are corrected for the slight change in kinematic viscosity which occurs as the density is varied. The data for pure water appear at effective particle density $\rho_{\mathrm{eff}} = 1.06$, and reflect the strong underestimate of particle accelerations with large dense particles. If the suppression of a_0 were due to density mismatch, the effect would reverse in the case where the particles are lighter than the fluid they displace, and the a_0 values would exceed the small particle limit. The data at $\rho_{\mathrm{eff}} = 0.96$ in figure 33 (taken at high salt concentration) show that although a_0 increases somewhat, it still remains far below the small-particle limit of 6 as seen in figure 32. These data demonstrate that for our measurements the effective coarse graining by the finite size particles is more important than the differential buoyancy due to the density mismatch in our experiment.

A simple model based on the K41 phenomenology can be used to predict the scaling of the acceleration with particle size in this regime where density mismatch is not important. We assume that the effect of finite particle size is that only flow structures larger than the particle size contribute to the acceleration. This means that the scaling of the acceleration variance can be determined by starting with $\langle a_x^2 \rangle \sim \epsilon^{3/2} \nu^{-1/2}$, and replacing the viscosity with the value that would make the Kolmogorov scale equal to the particle diameter, $\nu \to \epsilon^{1/3} d^{4/3}$. Consequently, the acceleration variance should scale as $d^{-2/3}$ for large particle sizes. We expect that below some particle size this scaling is no longer adhered to, and the acceleration becomes independent of particle size. The solid line in figure 32 shows the $d^{-2/3}$ scaling. There are not enough data to confirm this theory, but the data are consistent with this scaling. For large particle size, the data can be interpreted as following the $d^{-2/3}$ scaling, and for particle size less than 100 μm (5η) there is a change over to the acceleration being independent of particle size.

To provide an upper limit on the possible deviation of tracer particle acceleration

from that of fluid particles, we note that the dependence of a_0 on particle diameter in figure 32 could be interpreted as being roughly linear. An extrapolation of the linear dependence to zero particle size indicates that the acceleration variance of the 46 μm particles used for the acceleration measurements reported above is within 7% of that of fluid particles. This is really a worst case scenario, since the values obtained for 26 μm and 46 μm particles are indistinguishable within experimental uncertainties, and it is expected that the particle size dependence has zero slope at the origin. Note that these data are at the largest Reynolds number reported in this paper, and the particle size dependence will be weaker at lower Reynolds numbers. We conclude that the 46 μm particles are small enough to measure the acceleration variance at the 10% accuracy which we have reported.

6. Conclusion

We have reported high-resolution measurements of the Lagrangian properties of a high-Reynolds-number turbulent flow. The particle tracking system, based on the CLEO III silicon strip detector, is able to measure positions with spatial resolution of 0.5 μm (1/40 of the Kolmogorov distance, or 1/6400 of the field of view) and temporal resolution of 14 μs (1/20 of the Kolmogorov time) in an $R_\lambda = 970$ flow.

The primary results of this paper concern the fluid particle accelerations. We tested the long-standing Heisenberg–Yaglom prediction that the acceleration variance scales as $\epsilon^{3/2}$ (or $\tilde{u}^{9/2}$). At low Reynolds number, our data are consistent with DNS. However, we find that for $500 \geqslant R_\lambda \geqslant 970$ the value of a_0 is approximately constant, indicating that K41 theory approximates the acceleration scaling in this range of R_λ well. Turbulent intermittency models generally predict a very weak dependence of a_0 on Reynolds number (for example, $R_\lambda^{0.135}$ in Borgas' model) but experimental uncertainty currently makes it impossible to test such predictions.

The fact that the flow between counter-rotating disks has a well-defined anisotropy allows us to test the coupling of the acceleration to the structure of the large-scale flow. While the velocity exhibits a significant anisotropy which is independent of Reynolds number, the acceleration exhibits a smaller anisotropy which decreases as the Reynolds number is increased, as shown in figure 27.

The autocorrelation function of the acceleration component was also measured. Because of measurement volume effects, this measurement was restricted to relatively high Reynolds numbers. The functions are narrower than low-R_λ direct numerical simulations, and exhibit Kolmogorov scaling of the time.

The acceleration is found to be an extremely intermittent variable, as evidenced by the very long stretched exponential tails of the acceleration component PDF, shown in figures 19 and 21. The level of intermittency, reflected in the acceleration component flatness, is found to increase with Reynolds number. This is consistent both with the general expectation that turbulent intermittency should increase as the width of the scaling range increases, and with DNS measurements of the flatness at low Reynolds number.

The fast temporal response of the particle tracking system allows us to resolve the extremely violent events that make up the tails of the acceleration component PDF. The trajectory in figure 1 represents one such event, in which the particle acceleration rises to $16\,000\,\mathrm{m\,s^{-2}}$, 1600 times the acceleration due to gravity, and 40 times the r.m.s. value. Although we do not have quantitative evidence, we make the observation that the high-acceleration events appearing in the tails of the acceleration distributions (such as figure 1) seem to be associated with coherent structures which

persist for many Kolmogorov times, substantially longer than the correlation time of the acceleration components.

Particular attention has been paid to the determination of measurement errors. We have developed a numerical simulation of the detection process that takes input trajectories and models the optics and electronics to create artificial data. Using this approach we have measured the extrapolation error in the acceleration variance data and corrected for it. We have also confirmed that our analysis codes and choices for the analysis parameters are not biasing the results.

The dependence of the particle acceleration variance on the tracer particle size and density was also measured. It is found that the acceleration observed with 46 µm diameter polystyrene particles is within 7% of the value that would be obtained from ideal fluid particles, even at the highest Reynolds numbers studied. We find that particles of diameter 450 µm (26η) have an acceleration variance that is a factor of 3.6 smaller than fluid particles. In our experiment, this is caused primarily by the size of the particles and is only slightly affected by their density mismatch with the fluid. These measurements validate our Lagrangian acceleration measurements, and in addition they highlight the need for a deeper understanding of the motion of large density-matched particles in turbulence.

The techniques and measurements presented in this paper suggest many possibilities for the future development of optical particle tracking in turbulence. The use of high-resolution imaging equipment and careful attention to measurement errors will continue to be essential in future measurements. Possible extensions of the techniques presented here include lengthening the tracking times, improving the resolution of the three-dimensional measurements and tracking larger numbers of particles simultaneously. These will allow precise high-Reynolds-number experimental measurements of additional quantities including relative dispersion, scaling in the inertial time range, and the geometry of multi-particle Lagrangian motion.

Appendix A. Extraction of particle tracks from intensity data

The raw data from the strip detector consist of a series of one-dimensional intensity profiles taken at regular time intervals. The task of recognizing peaks in these intensity profiles and assembling them into two-dimensional or three-dimensional tracks is, in principle, similar to the case of two-dimensional CCD images (Virant & Dracos 1997; Ott & Mann 2000; Dracos 1996). However, the strip detector poses unique challenges. Particle tracks cross much more often in one-dimensional than in two-dimensional, and flaws in the detector lead to a number of inoperative strips. Both of these effects cause frequent drop-outs in tracks, which would result in fragmentation of the trajectories.

The strategy for extracting tracks from the intensity data is as follows. The task

is divided into four phases: peak detection, track building, track splicing and track filtering. In cases where two-dimensional trajectories are investigated, the tracks are then passed to a matching algorithm which associates x and y tracks to form two-dimensional trajectories.

Peak Detection. The algorithm scans each frame and identifies distinct groups of above-threshold strips, and searches each group for one or more peaks, taking into account the existence of inoperative strips. Valid peaks are passed to a routine which calculates moments of the peak and fits it to a Gaussian function, returning properties including peak centre, amplitude, full-width at half-maximum, area skewness and flatness. The output of the peak detection algorithm is a list of peaks for each frame.

Track Building. The track finding algorithm assembles the peaks found by the peak detector into time-continuous tracks. This algorithm builds tracks incrementally, extrapolating each track forward one frame and searching for a peak which is the continuation of the track. If any ambiguity is found – if there is more than one peak which might continue the track, or if there is more than one track which might continue onto a peak – the track building algorithm fails to resolve the match and begins new tracks as necessary.

Splicing. The list of tracks generated by the track builder is passed to a splicer which connects track fragments which the track builder failed to connect due to ambiguities. Such ambiguities are quite common in one-dimensional projection, since tracks can cross in one-dimensional projection even when the two-dimensional trajectories are distinct. The track builder looks more than one frame ahead, and compares forward extrapolations of the ends of tracks to backward extrapolations of the beginnings of tracks. It uses an iterative algorithm to make the best matches, while leaving ambiguous matches unresolved.

Filtering. After the splicing algorithm has exited, the tracks are processed by a filtering algorithm. The algorithm will delete data points which meet certain criteria. These criteria include upper and lower limits on the amplitude, and upper limits on the width and flatness of the peak. The algorithm also deletes data points which coincide with a list of inoperative strips. The idea is to keep marginally accurate data during the track assembly process to maintain the continuity of the tracks, but to exclude such data from subsequent statistical analysis, where the large uncertainties could be detrimental to the analysis.

Coordinate matching. Most of the acceleration data reported below are derived from two-dimensional trajectories. To obtain two-dimensional trajectories, it is necessary to match the x vs. t and z vs. t trajectories which are obtained from the two strip detectors. All such data are taken in the configuration shown in figure 5(a), in which the same image is projected on two strip detectors, and only the segments of tracks that lie in the overlap region of the two detectors (see figure 7) are used. In this case, the optical intensity recorded by the two detectors for a single track is highly correlated. The autocorrelation function between the two trajectories is therefore a good means for matching the tracks.

Appendix B. Reinterpretation of previous data

The data presented in this paper should be compared with previously published measurements of the same quantities in the same turbulent flow, but using a conventional position-sensitive photodiode instead of the strip detector to measure particle trajectories (Voth *et al.* 1998). The previous study reached the correct conclusion that the Heisenberg–Yaglom scaling of the acceleration variance is observed at high

Reynolds numbers, but because of limitations of the detector technology the numerical values obtained for the physical quantities involved were inaccurate.

The discrepancy can be largely attributed to the high noise level in the position-sensitive photodiode that resulted in much greater uncertainty in the particle position measurements and which necessitated the use of much larger tracer particles. The intrinsic bandwidth of the UDT DLS-10 position-sensitive photodiode used in the previous experiments is approximately 5 MHz, but temporal averaging of the signal was used to increase the effective position resolution at the expense of temporal resolution. Signal averaging with an effective bandwidth of 100 kHz was used in conjunction with tracer particles of diameter 250 μm or 450 μm, which gave a position resolution of 10 μm over a field of 1.5 mm, corresponding to a dynamic range of 150. By contrast, the strip detector at 70 kHz has a position uncertainty of approximately 0.1 strips on a field of 512 strips (0.8 μm over a field of 4 mm), giving a dynamic range of 5000, which is a factor of 30 improvement. Another critical advantage of the strip detector is that it is able to make these position measurements with 46 μm diameter particles. As reported in §5 above, the 250 μm particles which were required by the position-sensitive photodiode do not follow the flow at high Reynolds number and result in a significant underestimate of the acceleration.

The position-sensitive photodiode is strictly limited to single-particle statistics, so that the energy dissipation could not be measured in terms of velocity structure functions. Instead, the acceleration autocorrelation function was compared with DNS results to estimate the Kolmogorov time, and this value was used to determine the rate of energy dissipation. Presumably due to the fact that the 250 μm particles did not adequately follow the flow, the estimate of the Kolmogorov time was a factor 2.37 larger than the current value, and using $\tau_\eta = (v/\epsilon)^{1/2}$, this gave an estimate of the energy dissipation which is a factor 5.63 below the current value at a given propeller speed. The r.m.s. velocity $\tilde{u}$ was also underestimated by 10% in the old experiment, and using equation (3.7) the new values obtained for R_λ are smaller than the old by a factor of 0.52, so the previously reported range of R_λ (985–2021) would correspond to (512–1037) using the new calibration. The ability to work at much smaller R_λ (down to 140) results from the use of smaller particles, which do not settle out of the flow even at very slow propeller speeds.

The Kolmogorov constant a_0 is calculated from

$$a_0 = \langle a_i^2 \rangle \frac{v^{1/2}}{\epsilon^{3/2}} \qquad (B\,1)$$

and is also affected by this inaccuracy in the estimate of ϵ, and would have increased the value of a_0 by a factor of 17. However, the particle size effects and low spatial resolution caused the acceleration variance to be underestimated by a large factor. In the old study, an extrapolation to zero fit time was attempted, but large position errors obscured the exponential dependence of acceleration variance on fit time that is seen in figure 23. What was interpreted as 'measurement noise' was in reality a blend of measurement error and short-time turbulence contributions. The algorithm used to calculate the acceleration variance gave a value which was effectively coarse grained over a time interval which was believed to be $2.5\tau_\eta$ using the old calibration, but which is actually $6\tau_\eta$ using the new calibration. As may be seen from figure 23, this results in a substantial underestimate of the acceleration variance. The acceleration variance was further reduced by the particle size effect associated with the use of 250 μm particles. The fact that the value of a_0 reported in the previous experiment (7 ± 3) is close to the value now reported (≈ 6) is due to the fortuitous cancel-

lation of errors in the measurement of the dissipation rate and of the acceleration variance.

REFERENCES

AUMAITRE, S., FAUVE, S. & PINTON, J. F. 2000 Large scale correlations for energy injection mechanisms in swirling turbulent flows. *Eur. Phys. J.* B **16**, 563–567.

BASSET, A. B. 1888 On the motion of a sphere in a viscous liquid. *Phil. Trans. R. Soc. Lond.* A **179**, 43–63.

BECK, C. 2001*a* Dynamical foundations of nonextensive statistical mechanics. *Phys. Rev. Lett.* **87**, 180601–1 180601–3.

BECK, C. 2001*b* On the small-scale statistics of Lagrangian turbulence. *Phys. Lett.* A **287**, 240–244.

BELIN, F., MAURER, J., TABELING, P. & WILLAIME, H. 1996 Observation of intense filaments in fully developed turbulence. *J. Phys. Paris* II **6**, 573–584.

BELIN, F., MAURER, J., TABELING, P. & WILLAIME, H. 1997 Velocity gradient distributions in fully developed turbulence: An experimental study. *Phys. Fluids* **9**, 3843–3850.

BORGAS, M. S. 1993 The multifractal Lagrangian nature of turbulence. *Phil. Trans. R. Soc. Lond.* A **342**, 379–411.

BUCHAVE, P., GEORGE, W. K. & LUMLEY, J. L. 1979 The measurement of turbulence with the laser-Doppler anemometer. *Annu. Rev. Fluid Mech.* **11**, 443–503.

CADOT, O., DOUADY, S. & COUDER, Y. 1995 Characterization of the low-pressure filaments in a three-dimensional turbulent shear flow. *J. Phys.* **7**, 630–646.

CORRSIN, S. & LUMLEY, J. 1956 On the equation of motion for a particle in turbulent fluid. *Appl. Sci. Res.* **6**, 114–116.

DOUADY, S., COUDER, Y. & BRACHET, M. E. 1991 Direct observation of the intermittency of intense vorticity filaments in turbulence. *Phys. Rev. Lett.* **67**, 983–986.

DRACOS, T. 1996 *Three-Dimensional Velocity and Vorticity Measuring and Image Analysis Techniques.* Kluwer.

FAUVE, S., LAROCHE, C. & CASTAING, B. 1993 Pressure fluctuations in swirling turbulent flows. *J. Phys. Paris* II **3**, 271–278.

GOTOH, T. & FUKAYAMA, D. 2001 Pressure spectrum in homogeneous turbulence. *Phys. Rev. Lett.* **86**, 3775–3778.

GOTOH, T. & ROGALLO, R. S. 1999 Intermittancy and scaling of pressure at small scales in forced isotropic turbulence. *J. Fluid Mech.* **396**, 257–285.

HEISENBERG, W. 1948 Zur statistichen theorie der turbulenz. *Z. Phys.* **124**, 628–657.

HILL, R. J. 2001 Scaling of acceleration in locally isotropic turbulence. *J. Fluid Mech.* **452**, 361–370.

HILL, R. J. 2002 Possible alternative to R_λ scaling of small-scale turbulence statistics. *J. Fluid Mech.* **463**, 403–412.

HILL, R. J. & WILCZAK, J. M. 1995 Pressure structure functions and spectra for locally isotropic turbulence. *J. Fluid Mech.* **296**, 247–269.

HOLZER, M. & SIGGIA, E. D. 1993 Skewed, exponential pressure distributions from Gaussian velocities. *Phys. Fluids* **5**, 2525–2532.

KIT, E., TSINOBER, A. & DRACOS, T. 1993 Velocity gradients in a turbulent jet flow. *Appl. Sci. Res.* **51**(1-2), 185–1900.

KOLMOGOROV, A. N. 1941*a* Dissipation of energy in the locally isotropic turbulence. *Dokl. Akad. Nauk SSSR* **31**, 538–540.

KOLMOGOROV, A. N. 1941*b* The local structure of turbulence in incompressible viscous fluid for very large Reynolds numbers. *Dokl. Akad. Nauk SSSR* **30**, 301–305.

KURIEN, S. & SREENIVASAN, K. R. 2000 Anisotropic scaling contributions to high-order structure functions in high-Reynolds-number turbulence. *Phys. Rev.* E **62**, 2206–2212.

LA PORTA, A., VOTH, G. A., CRAWFORD, A. M., ALEXANDER, J. & BODENSCHATZ, E. 2001 Fluid particle accelerations in fully developed turbulence. *Nature* **409**, 1017–1019.

LA PORTA, A., VOTH, G. A., MOISY, F. & BODENSCHATZ, E. 2000 Using cavitation to measure statistics of low-pressure events in large-Reynolds-number turbulence. *Phys. Fluids* **12**, 1485–1496.

MAURER, J., TABELING, P. & ZOCCHI, G. 1994 Statistics of turbulence between two counter-rotating disks in low-temperature helium gas. *Europhys. Lett.* **26**, 31–36.

Maxey, M. R. & Riley, J. J. 1983 Equation of motion for a small rigid sphere in a nonuniform flow. *Phys. Fluids* **26**, 883–889.

Monin, A. S. & Yaglom, A. M. 1975 *Statistical Fluid Mechanics*, vol. 2 (ed. J. L. Lumley). MIT Press.

Mordant, N., Metz, P., Michel, O. & Pinton, J. 2001 Measurement of Lagrangian velocity in fully developed turbulence. *Phys. Rev. Lett.* **87**, art. no. 214501.

Noullez, A., Wallace, G., Lempert, W., Miles, R. B. & Frisch, U. 1997 Transverse velocity increments in turbulent flow using the relief technique. *J. Fluid Mech.* **339**, 287–304.

Ott, S. & Mann, J. 2000 An experimental investigation of relative diffusion of particle pairs in three-dimensional turbulent flow. *J. Fluid Mech.* **422**, 207–223.

Pope, S. B. 1994 Lagrangian PDF methods for turbulent flows. *Annu. Rev. Fluid Mech.* **26**, 23–63.

Pope, S. B. 2000 *Turbulent Flows*. Cambridge University Press.

Pratsinis, S. E. & Srinivas, V. 1996 Particle formation in gases, a review. *Powder Technol.* **88**, 267–273.

Sato, Y. & Yamamoto, K. 1987 Lagrangian measurement of fluid-particle motion in an isotropic turbulent field. *J. Fluid Mech.* **175**, 183–199.

Sawford, B. 2001 Turbulent relative dispersion. *Annu. Rev. Fluid Mech.* **33**, 289–317.

Shen, X. & Warhaft, Z. 2000 The anisotropy of the small scale structure in high Reynolds number ($R_\lambda \sim 1000$) turbulent shear flow. *Phys. Fluids* **12**, 2976–2989.

Shraiman, B. I. & Siggia, E. D. 2000 Scalar turbulence. *Nature* **405**, 639–646.

Skubic, P., Alexander, J., Arndt, K. *et al.* 1998 The CLEO III silicon tracker. *Nuclear Instrum. Meth. Phys. Res.* A **418**, 40–51.

Snyder, W. H. & Lumley, J. L. 1971 Some measurements of particle velocity autocorrelation functions in a turbulent flow. *J. Fluid Mech.* **48**, 41–71.

Sreenivasan, K. R. 1995 On the universality of the Kolmogorov constant. *Phys. Fluids* **7**, 2778–2784.

Vaillancourt, P. A. & Yau, M. K. 2000 Review of particle-turbulence interactions and consequences for cloud physics. *Bull. Am. Met. Soc.* **81**, 285–298.

Van Atta, C. W. & Antonia, R. A. 1980 Reynolds-number dependence of skewness and flatness factors of turbulent velocity derivatives. *Phys. Fluids* **23**, 252–257.

Vedula, P. & Yeung, P. K. 1999 Similarity scaling of acceleration and pressure statistics in numerical simulations of isotropic turbulence. *Phys. Fluids* **11**, 1208–1220.

Virant, M. & Dracos, T. 1997 3D PTV and its application on Lagrangian motion. *Meas. Sci. Technol.* **8**, 1539–1552.

Voth, G. A., La Porta, A., Crawford, A. M., Bodenschatz, E. & Alexander, J. 2001 A silicon strip detector system for high resolution particle tracking in turbulence. *Rev. Sci. Instrum.* **72**, 4348–4353.

Voth, G. A., Satyanarayan, K. & Bodenschatz, E. 1998 Lagrangian acceleration measurements at large Reynolds numbers. *Phys. Fluids* **10**, 2268–2280.

Yaglom, A. M. 1949 On the acceleration field in a turbulent flow. *C. R. Akad. URSS* **67**(5), 795–798.

Yeung, P. K. 2001*a* Lagrangian characteristics of turbulence and scalar transport in direct numerical simulations. *J. Fluid Mech.* **427**, 241–274.

Yeung, P. K. 2001*b* Lagrangian investigations of turbulence. *Annu. Rev. Fluid Mech.* **34**, 115–142.

Yeung, P. K. & Pope, S. B. 1989 Lagrangian statistics from direct numerical simulations of isotropic turbulence. *J. Fluid Mech.* **207**, 531–586.